LITHOS 400-401 (2021) 106432

Contents lists available at ScienceDirect

LITHOS

journal homepage: www.elsevier.com/locate/lithos

Research Article

Trace element fingerprints of Ni–Fe–S–As minerals in subduction channel serpentinites

José M. González-Jiménez [a,b,*], Rubén Piña [c], J. Edward Saunders [d], Gaëlle Plissart [e], Claudio Marchesi [a,b], José A. Padrón-Navarta [b,f], María Ramón-Fernandez [a], Leonardo N. F. Garrido [e], Fernando Gervilla [a,b]

[a] Departamento de Mineralogía y Petrología, Facultad de Ciencias, Universidad de Granada, Avda. Fuentenueva s/n, 18002 Granada, Spain
[b] Instituto Andaluz de Ciencias de la Tierra (IACT), CSIC-UGR, Avda. de las Palmeras 4, 18100 Armilla, Granada, Spain
[c] Departamento de Mineralogía y Petrología, Facultad de Ciencias Geológicas, Universidad Complutense de Madrid, C/ José Antonio Novais, 2, 28040, Madrid, Spain
[d] Division of Earth Sciences, School of Environmental and Rural Science, University of New England, Armidale, NSW 2351, Australia
[e] Instituto de Ciencias de la Tierra, Universidad Austral de Chile, Valdivia, Chile
[f] Géosciences Montpellier, CNRS & Université de Montpellier, Montpellier Cedex 5 F-34095, France

ARTICLE INFO

Keywords:
Subduction channel
Serpentinite
Base-metal mineral
Sulfides
Arsenides

ABSTRACT

A variety of base-metal minerals (BMM) may form during hydration-dehydration of ultramafic rocks within subduction zones. However, the trace element fingerprints of these minerals and their relation to different stages of the subduction cycle are still unexplored. Here, we present the first comprehensive in situ analysis by Laser Ablation Inductively Coupled Plasma Mass Spectrometry (LA-ICP-MS) of (semi)-metals (Ni, Fe, As, Sb, Co, Bi, Te, Pb, Cd, Se, Cu, Zn, and Mn) and precious metals (Os, Ir, Rh, Pt, Pd, Au, and Ag) for Ni–Fe–S–As minerals in subducted serpentinites from the La Cabaña area (South-Central Chile). The targeted rocks are medium- and high-pressure serpentinites recording the entire cycle of burial-exhumation within a subduction zone. A first stage of hydration of upper mantle peridotites within the mantle wedge led to formation of lizardite after magmatic olivine at ~300 °C. This stage was followed by prograde hydration (i.e., antigoritization at ~320–400 °C; <1GPa) and subsequent partial dehydration (formation of prograde olivine at ~600 °C and 1.1 GPa) within the subduction channel, and final exhumation of the serpentinites and incorporation in the accretionary prism still in the stability field of antigorite (>300 °C). The Ni–Fe–S–As minerals in these serpentinites include Ni-Fe-rich sulfides [pentlandite $(Ni,Fe)_9S_8$), smythite (Fe_9S_{11}), heazlewoodite (Ni_3S_2), millerite (NiS)], arsenides [orcelite ($Ni_{5-x}As_2$), nickeline (NiAs) and maucherite ($Ni_{11}As_8$)] and, to a lesser extent, alloy (awaruite, Ni_3Fe) and sulfarsenides (gerdorffite, NiAsS). Their abundance, morphology and chemistry strongly vary with the degree of serpentinization and style of deformation of the host rock. Thus, euhedral grains of heazlewoodite ± awaruite ± magnetite formed in equilibrium with lizardite when magmatic olivine was hydrated within the mantle wedge. Once the lizardite-olivine serpentinites were incorporated into the subduction serpentinite channel, the infiltration of hotter (S-As-Sb)-bearing fluids promoted antigoritization under static regime and precipitation of orcelite and pentlandite in equilibrium with antigorite. Channelling of fluids in zones of focussed strain enhanced further antigoritization in some schistose serpentinites at decreasing fO_2 and fS_2, resulting in the transformation of pentlandite into a second generation of heazlewoodite–awaruite–magnetite. After relic olivine exhaustion, fO_2 and fS_2 increased promoting the replacement of the secondary heazlewoodite to millerite. No significant variations in terms of trace elements were observed during these mineral replacements associated to hydration upon prograde metamorphism and/or increasing of strain. In contrast, partial dehydration of serpentinites under high-pressure conditions (> 1GPa) generated Ni-rich awaruite in equilibrium with the prograde assemblage antigorite-metamorphic olivine. These awaruites are depleted in trace elements, indicating substantial (semi)-metal and precious metal mobility during high P-T metamorphism within the subduction channel. During the final stage of deformation linked to exhumation inside the accretionary prism some orcelite grains formed during early antigoritization recrystallized without substantial change in trace element concentration. At

* Corresponding author at: Departamento de Mineralogía y Petrología, Facultad de Ciencias, Universidad de Granada, Granada, Avda. Fuentenueva s/n 18002, Spain.
E-mail address: jmgonzj@ugr.es (J.M. González-Jiménez).

https://doi.org/10.1016/j.lithos.2021.106432
Received 2 March 2021; Received in revised form 16 August 2021; Accepted 17 August 2021
Available online 23 August 2021

this stage, nickeline singularly enriched in gold formed in equilibrium with the recrystallizing orcelite. These results demonstrate that Ni–Fe–S–As minerals formed or modified during the entire subduction cycle of upper mantle rocks have their own characteristic trace element signature (i.e., depletion in precious metals and enrichment in As, Sb, Te, Bi and Pb) that distinguish them from magmatic counterparts.

1. Introduction

Subduction zones are sites that promote mass exchange between Earth's near-surface and deep reservoirs (e.g., Cannaò and Malaspina, 2018). In these geological settings, the subduction of altered oceanic or continental lithosphere promotes the transference of water and other components from the subducting plate back to the overlying mantle wedge and, eventually, the arc crust. The nature of the interface between the subducting and overlying plates governs the efficiency of this geochemical transfer, which in turns strongly varies depending on the thermal structure of the subducting system (Guillot et al., 2015). In cold subduction zones, coherent slices of oceanic lithosphere may be potentially subducted and exhumed by the formation of serpentinized fronts mostly localized in the subducting plate, as proposed for ophiolites in the Alps (for a comprehensive review see Agard, 2021). In contrast, in hot subduction zones, both the lower and upper plates are serpentinized by fluids released upwards, giving rise to a very distinct structure of the plate interface. Geophysical imaging (e.g., Hyndman and Peacock, 2003) along with petrological (e.g., Blanco-Quintero et al., 2011) and numerical modeling (Gerya et al., 2002) show that at >30 km such slab-mantle wedge interface consists of a 2–10 km thick layer of serpentinites (Gerya et al., 2002; Guillot et al., 2001). This serpentinite layer, which may extend up to 100 km depth, is known in the literature as the subduction channel and corresponds to a tectonic mélange with blocks of variable lithology and provenance (Bebout, 2007; Gerya et al., 2002). These mélanges may include serpentinites derived from both the subducting slab ("subducted serpentinites") and the upper plate, formed prior to subduction in a range of geodynamic settings, including mid-ocean ridges, abyssal transform-faults, ocean-continent transition zones and passive margins and slab bending near the trench, or serpentinites derived from the upper plate and thus the mantle wedge (Blanco-Quintero et al., 2011; Deschamps et al., 2013; Hattori and Guillot, 2003, 2007; Scambelluri et al., 2001). Thus, the subduction channel is composed of serpentinites from various origins whose composition will further evolve due to fluid/rock interactions, with fluids that can derived from metasediments, oceanic crust and/or the subducted mantle.

Upon subduction of the slab, serpentinites experience prograde metamorphism. First, the low-temperature varieties of serpentine, namely chrysotile and lizardite, transform to antigorite (~ 300 °C) and subsequently antigorite breakdowns to secondary olivine and finally to olivine + orthopyroxene + chlorite at around 600–650 °C and 120–200 km depths (Padrón-Navarta et al., 2011; Trommsdorff et al., 1998). All these reactions imply dehydration and liberation of fluids with variable element cargoes. At relatively shallow depths (< 120–160 km) these fluids may be transferred directly to the overlying mantle wedge (e.g., Hattori and Guillot, 2003; Paulatto et al., 2017) or travel parallel to the slab (Piccoli et al., 2021). In contrast, at greater depths, melts derived from the partial melting of mélanges consisting of serpentinites mixed with slab material (including hydrated sediments, continental/oceanic crustal basalts and gabbros) seem to govern the transfer of elements to the supra-subduction zone mantle wedge (Castro and Gerya, 2008; Gerya and Yuen, 2003; Proenza et al., 2018).

Available bulk-rock data of subduction channel serpentinites worldwide indicate that they can be enriched in elements transferred to arc magmas, which in some cases may produce economically important ores. These include halogens such as F and Cl (Debret et al., 2014; Kendrick et al., 2011), the volatiles C, B, S and Se (Alt et al., 2012, 2013; Alt and Shanks, 2003; Harvey et al., 2014; Scambelluri and Tonarini, 2012), lithophiles such as LREE, V, Zn, Cr, Ti (Deschamps et al., 2013; Hattori and Guillot, 2003), the chalcophiles As, Sb, Sn, Mo, Co (Deschamps et al., 2013; Hattori and Guillot, 2003), the moderately siderophiles Ni, Co (Deschamps et al., 2010) and the highly siderophile elements Pt, Pd, Re, Au, and Ag (Rielli et al., 2018). Some of these elements (e.g., F, Cl, As, Sb and S), which are concentrated in serpentinites from a few ppb to thousands of ppm amounts, may be incorporated during hydration of mantle peridotites at any stage of their evolution, including during subduction by fluid interaction with subducted sediments (Deschamps et al., 2010, 2011, 2013; Hattori and Guillot, 2003, 2007; Scambelluri et al., 2001). Therefore, subduction channel serpentinites may transfer elements to deeper and hotter levels in the mantle than other subducted rocks.

Crossley et al. (2020) have recently measured precious metals (Os, Ir, Ru, Rh, Pt, Pd, Au and Re) in Ni—Fe sulfides (pentlandite, heazlewoodite and pyrite) of subducted serpentinites from Alpine Corsica by Laser Ablation Inductively Coupled Plasma Mass Spectrometry (LA-ICP-MS), confirming a mineral-scale depletion of these elements during prograde metamorphism. The mobility of precious metals is apparently related to the destabilization of pre-existing magmatic sulfides and metal concentration into fluids migrating to the mantle wedge. In situ measurements of precious metals in metasomatic sulfides from mantle wedge peridotites seem to confirm the recycling of these metals by slab-derived fluids produced by dehydration of serpentinites (Rielli et al., 2018). These metasomatic sulfides may also be an important repository for Ag and other siderophile (Ni and Co) and chalcophile elements (As, Se, Sb, Te, Bi, Pb, Zn and Mn), with concentrations varying in the range of sub-ppm to a few wt% (Hattori et al., 2002). In addition, Co-Ni-As sulfarsenides predominate the opaque mineralogy of some subducted serpentinites with different metamorphic grade from the Alps (e.g., Oberengadin and Val Malenco; Buckahr, 1989). However, at the present there is no data on trace element signature neither in sulfides and alloys nor in sulfarsenides from subduction channel serpentinite

This work aims to determine by LA-ICP-MS the mineral repositories of (semi)-metals and precious metals and constrain the mechanisms of their mobility in serpentinites by studying Ni-Fe-As-S minerals in a fossil serpentinitic subduction channel from the La Cabaña area, South-Central Chile. Petrography and major element mineral chemistry determined by Electron Probe Micro Analyzer (EPMA) are employed to define mineral paragenesis for a suite of serpentinized mantle peridotites of variable metamorphic grade, with a special focus on Ni-Fe-S-As minerals, including Ni-rich sulfides (pentlandite, heazlewoodite and millerite), alloys (awaruite), arsenides (orcelite and nickeline) and sulfarsenides (gersdorffite).

2. Geological and petrostructural background of the samples

2.1. Outcrops of ultramafic rocks in the Coastal Cordillera of Chile

The partially to completely serpentinized peridotites investigated in this study are located approximately 60 km north-west of the Temuco city, within the so-called area of La Cabaña in South-Central Chile (Fig. 1a). This area is the largest cluster of meta-ultramafic rocks of the Coastal Cordillera of Chile and includes several serpentinite bodies (<1 km^2) known as Centinela Bajo Norte, Centinela Bajo Sur, Lavanderos, Loma Guzmán and Encanto River (Fig. 1b; González-Jiménez et al., 2014, 2016, 2017; Romero et al., 2018; Plissart et al., 2019).

The Coastal Cordillera of Chile is a paired metamorphic belt interpreted as a fossil accretionary wedge developed at the end of the

Palaeozoic on the western margin of Gondwana (Hyppolito et al., 2014a, 2014b; Romero et al., 2020; Willner, 2005), which extends almost continuously between 32° S and 43° S along the Pacific Coast of Chile (Fig. 1a). The Eastern Series of this metamorphic belt consists of slightly deformed continental-derived sedimentary rocks metamorphosed under high-temperatures and low-to-intermediate pressure owing to the intrusion of the Coastal Batholith between 320 and 300 Ma (Deckart et al., 2014; Willner, 2005). In contrast, the Western Series comprises rocks of continental (metapelites and metapsammites) and oceanic-related origins (metasediments, metavolcanics, metagabbros and serpentinized peridotites), recording higher pressure and lower temperature (*HP–LT*) metamorphism. Most of these rocks experienced metamorphism in the transition between the greenschist and lower blueschist facies (peak conditions at 0.70–0.93 GPa, 380–420 °C; Willner, 2005), although some isolated blocks of garnet–micaschists (1.25–1.4 GPa and 540–580 °C; Hyppolito et al., 2014a, 2014b), blueschists (0.95–1.07 GPa and 350–385 °C, Willner, 2005) and eclogite-facies serpentinite (2.0–2.5 GPa and < 600 °C; González-Jiménez et al., 2017) record higher peak conditions.

Previous studies proposed confronted hypotheses about the origin of the meta-ultramafic rocks of the Western Series. In particular, the ultramafic rocks of La Cabaña have been interpreted as remnants of a mantle portion originally located beneath an ocean ridge or an intra-oceanic back-arc mantle later metamorphosed in a subduction zone (Höfer et al., 2001 and references therein). Recent works based on a combination of multi-scale structural data with comprehensive mineralogical, petrological, geochemical and geochronological analyses have confirmed this hypothesis (González-Jiménez et al., 2014, 2016, 2017; Romero et al., 2018; Plissart et al., 2019; González-Jiménez et al. (2016), and highlighted that serpentinites from La Cabaña display trace-element profiles enriched in fluid-mobile elements (FME: As, Sb, B, Li, Cs, Pb, U, Ba, Sr), similar to meta-ultramafic rocks that underwent hydration in the mantle wedge above slabs (e.g., Deschamps et al., 2011). These authors suggested that peridotites originally sited in the back-arc of a supra-subduction zone were hydrated by slab-derived fluids, then buried and later exhumed within a subduction channel developed during the formation and evolution of the Central Chilean paleo-subduction zone in the Palaeozoic, ca. 380–280 Ma ago (González-Jiménez et al., 2014, 2016, 2017; Plissart et al., 2019; Romero et al., 2018).

2.2. Petrostructural background of the samples

For this study we have examined 150 polished thin sections from new (n = 8) and selected samples (n = 40) previously studied by González-Jiménez et al. (2014, 2016, 2017) and Plissart et al. (2019), which were collected in situ at various locations within the La Cabaña ultramafic bodies (Appendix 1). The base-metal minerals (BMM) were found in 16 of these studied samples comprising all the ultramafic lithotypes previously recognized in this area, namely partially serpentinized massive peridotites, schistose serpentinites and mylonitic serpentinites recognized from the Centinela Bajo Norte and Lavanderos bodies (Figs. 2a-b), as well as antigoritic massive serpentinites from the Loma Guzmán body, described here for the first time. González-Jiménez et al. (2016, 2017) and Plissart et al. (2019) have studied in detail the petrologic and structural features of these rocks, and only a brief summary of their main characteristics is provided here.

The partially serpentinized massive peridotites are coarse-grained meta-dunites (formerly >90 vol% mantle olivine) and meta-harzburgites (locally grading to lherzolites) with variable contents of accessory chromite and pyroxene pseudomorphs (i.e., bastite), which are found in the field as decametric lenses hosted in antigoritic schistose serpentinites (Figs. 2a-b and 3a). In this type of rocks, a first event of hydration at ~300 °C under static regime promoted the replacement of mantle olivine by (20–80%) mesh-textured lizardite (+ dispersed magnetite) as well as the alteration of primary Cr-rich spinel (occasionally representing >10 vol% of the rock) to ferrian chromite and/or Cr-rich magnetite. Some of the samples, namely locally schistose partially serpentinized massive peridotite, exhibit a nascent foliation (S1) of secondary antigorite overprinting the lizardite mesh (Fig. 3b) related to a second hydration event at ~320–400 °C and < 1.0 GPa (Fig. 2b).

During the incorporation of the lizardite-olivine peridotite into the subduction channel, the infiltration of progressively hotter silica-rich fluids through zones that focused strain promoted the formation of

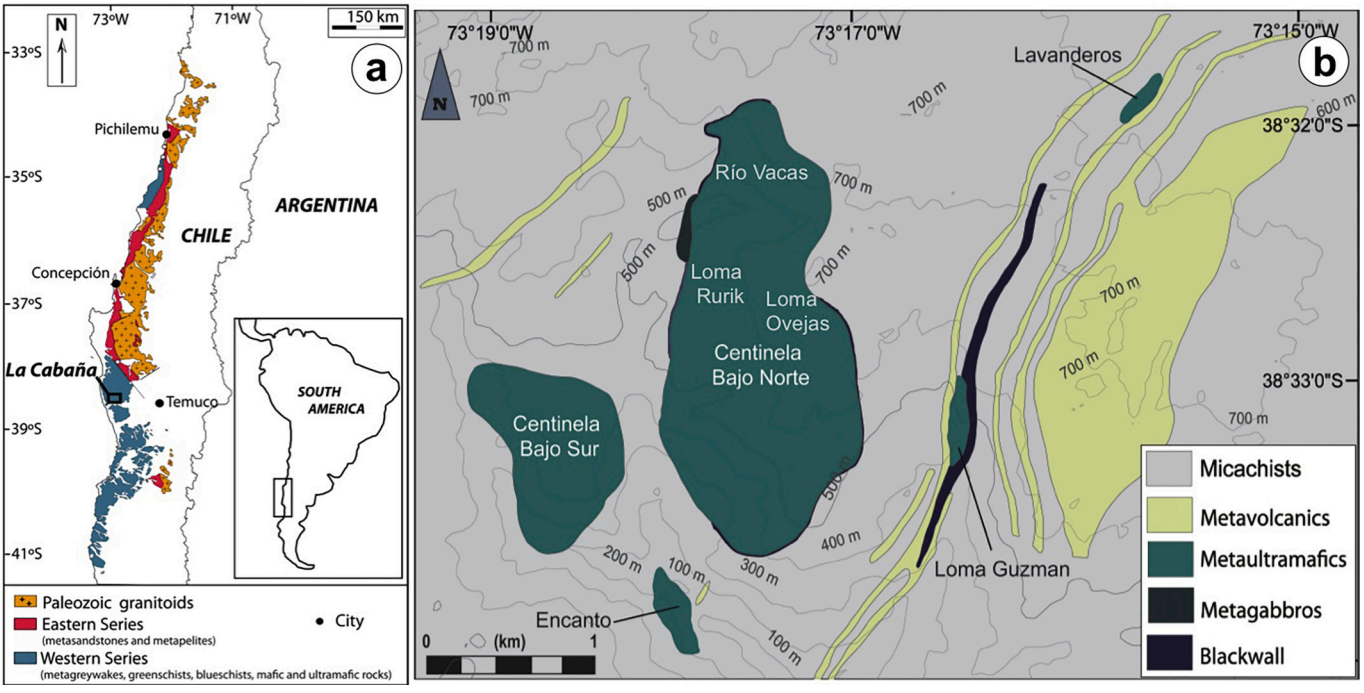

Fig. 1. (a) Geological setting and location of the study area in the Western Series (modified from Hervé et al., 2013). (b) Geological map of the La Cabaña area modified from Höfer et al. (2001), showing the location of the good outcrop exposures of meta-ultramafic rocks.

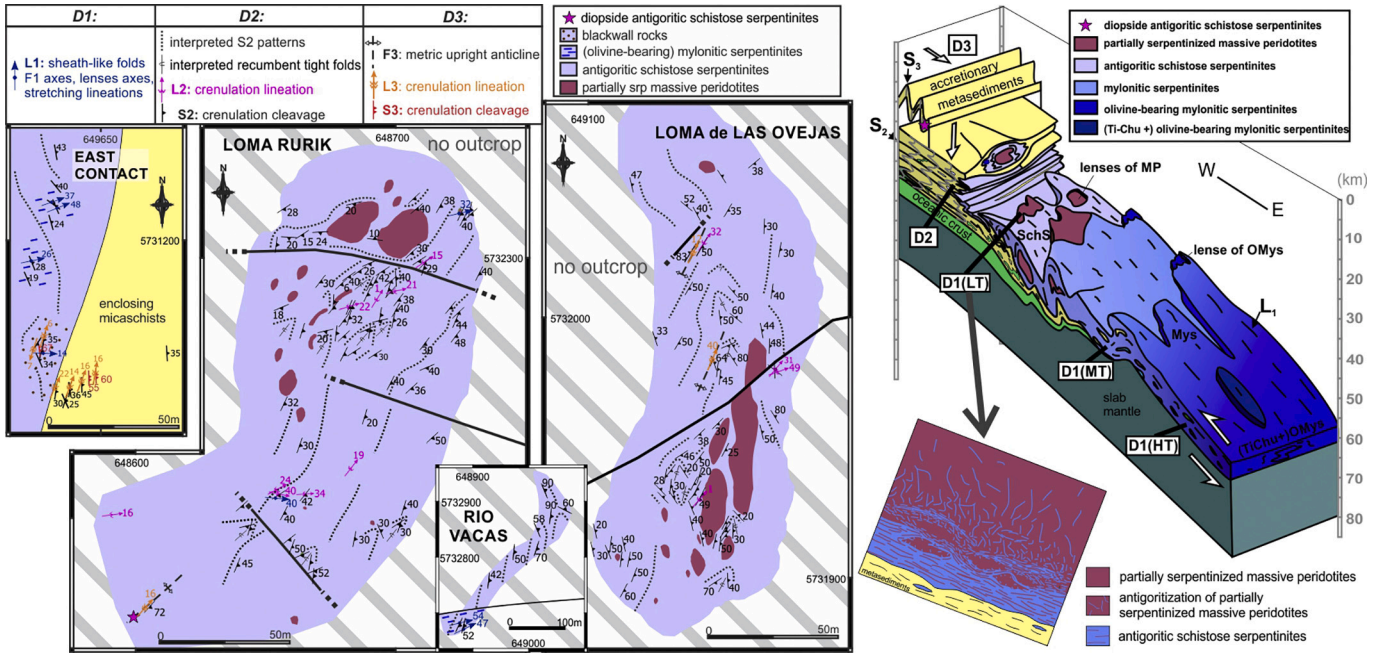

Fig. 2. (a) Structural maps of the Centinela Bajo Norte good exposures, displaying the three recognized ductile deformation phases in the meta-ultramafic rocks. (b) 3D sketch showing where the La Cabaña ultramafic lithotypes formed and their incorporation inside the shallow serpentinitic channel, in a context of subduction channel and accretionary prism, between 0 and 80 km depth. Structural map and view of the subduction channel architecture from Plissart et al. (2019).

antigoritic schistose serpentinites (Fig. 2a-b and 3c-d). This formed decametric sheath-like F_1 folds consisting of cores of partially serpentinized massive peridotites preserved amidst enclosing antigoritic schistose serpentinite (Fig. 2a-b). The antigoritic schistose serpentinites are the most abundant rocks at La Cabaña area (Fig. 2a) and, at the micro-scale, preserve ribbons of olivine replaced by mesh-textured lizardite ± magnetite and relic magmatic olivine (Fo = 89–93. NiO < 0.43 wt% and Mn < 0.26 wt%; Plissart et al., 2019) overgrown by antigorite defining the S1 foliation. In places, S1 was both transposed and crenulated (Fig. 3c-d) during a second (D2) event of folding (i.e., F2) giving rise to S2 foliation. This second phase of deformation was a subvertical shortening characterized by recumbent folds that overprints D_1 (Fig. 2a-b and 3c-d). This D2 deformation event is also identified in the enclosing micachist, timing the incorporation of the subducted serpentinites into the accretionary prism at ~280 Ma ago (Romero et al., 2018). Moreover, the matrix of antigoritic schistose serpentinites also host small bodies (10–20 m wide) of serpentinites displaying mylonitic fabric (Fig. 2a-b and 3e). In these rocks, magmatic olivine and mesh lizardite were fully replaced by antigorite at higher peak metamorphic conditions (up to ~600 °C and 1.10 GPa; Plissart et al., 2019). Mylonitic serpentinites consist of a matrix of elongated antigorite blades (defining foliation S1 and pronounced stretching lineation L1, characteristic of the D1 deformation inside the subduction channel) with relicts of accessory chromite and magnetite. At the micro-scale, the D1 matrix wraps around oriented lenses/ribbons giving rise to three mineralogical assemblages (Fig. 2a-b; Plissart et al., 2019): (1) mylonitic serpentinites sensu stricto made up of interpenetrating antigorite ± Cr-spinel ± magnetite, (2) olivine-bearing mylonitic serpentinites containing metamorphic olivine (+ antigorite + magnetite ± Cr-spinel ± dolomite, and (3) Ti-clinohumite and Ti-chondrodite + metamorphic olivine + magnetite ± Cr-spinel. Among these rocks, BMM were only identified in the olivine-bearing bearing mylonitic serpentinites (Fig. 3e). Olivine in these rocks has Fo = 90–97, NiO = 0.32–0.54 wt% and Mn = 0.10–0.66 wt% (Plissart et al., 2019).

A third deformation event (D_3) consisted of subhorizontal SE-NW shortening and is recorded in the La Cabaña ultramafic rocks as metric anticlines in a few outcrops of antigoritic schistose serpentinites with diopside (i.e., diopside-bearing antigoritic schistose serpentinites). This event also resulted in the upright folding of S_2 and development of a subvertical crenulation cleavage (S_3, Fig. 2a-b and 3d). In the Lavanderos outcrop, these rocks host small chromitite bodies recording a first metamorphic alteration event of chromite concomitant to prograde antigoritization at ~510–560 °C and a subsequent cooling event related to exhumation within the thermal interval of ~430–190 °C (González-Jiménez et al., 2016).

Antigoritic massive serpentinites identified in the Loma Guzmán body mainly consist of interpenetrating antigorite intergrown with magnesite (Fig. 3f).

3. Analytical methods

Polished thin-sections were first inspected under the optical microscope in reflected and transmitted light in an effort to characterize BMM and detect discrete minerals of noble metals (e.g., platinum-group minerals, PGM). The BMM and PGM were imaged and identified qualitatively by their characteristic Energy Dispersive Spectra (EDS) using a Leo Gemini Field Emission Scanning Electron Microscope (FE-SEM) belonging to the Centro de Instrumentación Científica of the Universidad de Granada, Spain. The instrument was equipped with SE, BSE and EDS detectors. Accelerating voltage was 20 kV and beam current was optimized for a sufficient number of counts for each EDS analysis. Once identified in the polished thin sections, major and minor-element compositions of BMM, including sulfides, sulfarsenides, arsenides and alloys, were obtained by wavelength-dispersive spectrometry (WDS) EPMA using a JEOL JXA-8230 at the Centres Científics i Tecnològics of the University of Barcelona (CCiTUB, Barcelona, Spain). An accelerating voltage of 15 keV and a beam current of 20 nA were used. All elements were measured with a counting time of 10 s for the peak. Calibration for analysis was performed using natural FeS for S and Fe, PbS for Pb, chalcopyrite for Cu, and chromite for Cr, synthetic InSb for Sb and GaAs for As, metallic Co for Co and metallic Ni for Ni; the X-ray lines employed were Kα for S, Fe, Co, Ni and Cr, Mα for Pb and Lα for Sb and As.

The in-situ trace-element analytical methodology of BMM followed, in a first round, that of Saunders et al. (2015; 2016). Analyses were done

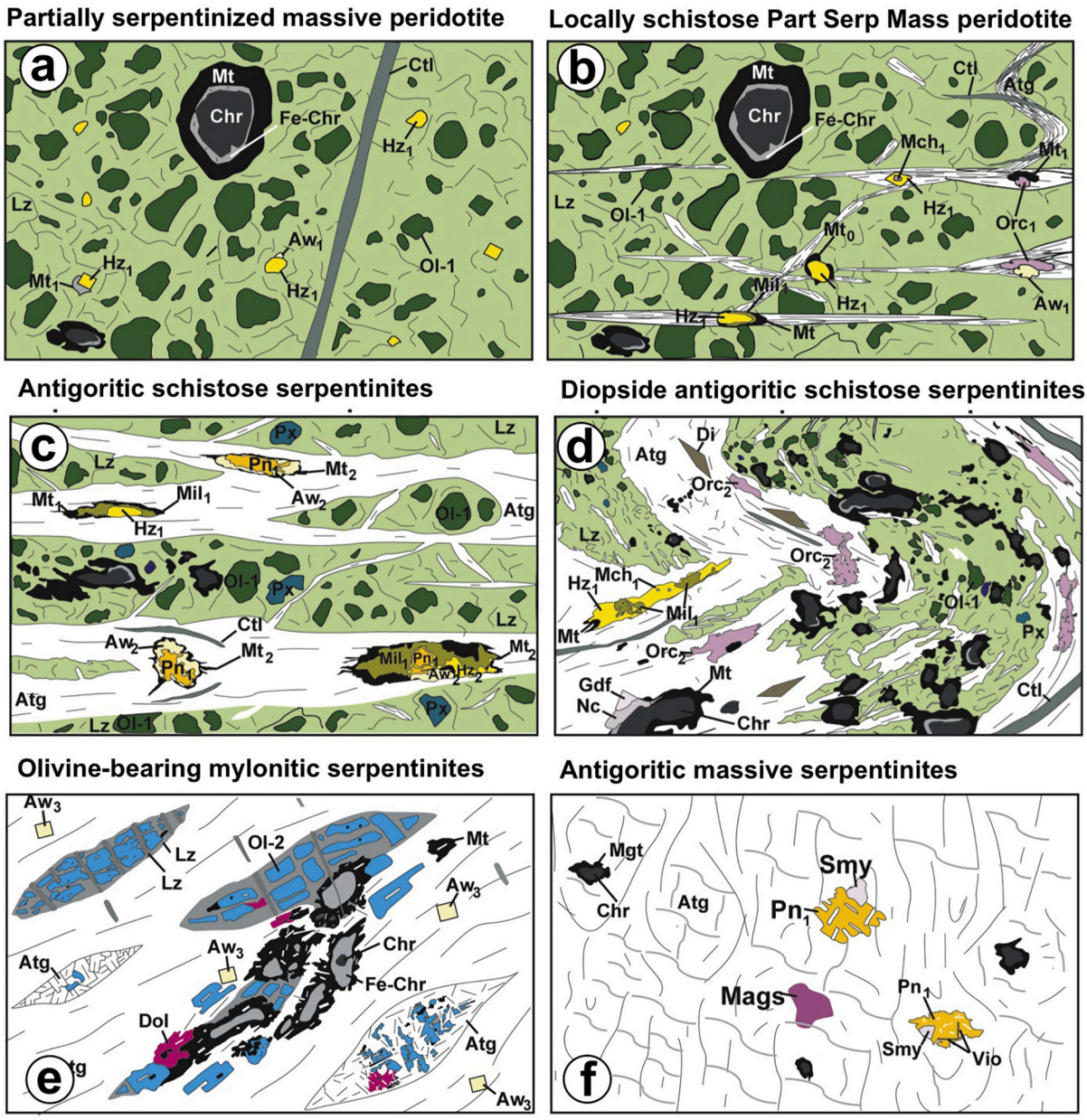

Fig. 3. Simplified drawings of representative microstructures and assemblages of meta-ultramafic rocks from the study area showing the localization of the opaque minerals. Partially serpentinized massive peridotites with no deformation and local schistosity are drawn in (a) and (b) respectively. Pictures (c) and (d) correspond to antigoritic schistose serpentinites. Foliation in (c) corresponds to S1 transposed to S2. Crenulation in (d) correspond to the D3 event, folding the S2 foliation. Note that D3 folds show an upright position. (e) Olivine-bearing mylonitic serpentinite containing euhedral grains of awaruite in the foliated antigorite matrix. (f) Antigoritic massive serpentinite hosting large grains of pentlandite partially altered to smythite ± violarite ± pyrite. Note that olivine-free mylonitic serpentinites and crenulated Ti-clinohumite and olivine-bearing serpentinites (not shown) do not contain Ni-rich opaque minerals.

on polished sections using an Agilent 7700cx inductively coupled plasma mass spectrometer coupled with a Photon Machines Excite 193 nm excimer laser ablation system (LA-ICP-MS) in the Geochemical Analysis Unit (GAU) at CCFS/GEMOC, Macquarie University, Sydney. Data were collected and processed using the GLITTER™ software (Griffin, 2008), which allows for the cleanest part of the time-resolved spectrum to be selected, avoiding inclusions of host silicates. Laser-ablation analysis of grains was carried out using He as the carrier gas, which was blended with Ar prior to introduction into the plasma. The laser system was operated at 5 Hz, with a laser energy of 5.69 J cm^{-2}. Spot sizes ranged from 40 to 50 μm. The monitored isotopes were ^{29}Si, ^{31}P, ^{34}S, ^{57}Fe, ^{59}Co, ^{60}Ni, ^{65}Cu, ^{75}As, ^{78}Se, ^{99}Ru, ^{101}Ru, ^{103}Rh, ^{105}Pd, ^{107}Ag, ^{111}Cd, ^{112}Cd, ^{121}Sb, ^{125}Te, ^{185}Re, ^{189}Os, ^{193}Ir, ^{195}Pt, ^{197}Au, ^{208}Pb, and ^{209}Bi. A quenched NiS bead (PGE-A: Saunders et al., 2016), doped with selected chalcophile and siderophile elements, was used as an external calibration standard for all elements with the exception of Sb. A chalcophile glass (IMER-2) was used for calibration of Sb concentrations. The accuracy of calibration was assessed using BCR-2 and IMER-2 glasses as unknowns. Sulfur, determined by EMP, was used as internal standard for LA-ICP-MS analyses of sulfides (pentlandite, heazlewoodite and millerite) to quantify the trace-element abundances. For the arsenide grains (orcelite), which are stoichiometric and homogenous, a Ni value of 65.14 wt% was used as internal standard for all grains.

A second round of in situ trace element analyses were carried out of

some of the previous samples also by LA-ICP-MS at LabMaTer (UQAC) using an Excimer 193 nm Resolution M-50 laser ablation system coupled to an Agilent 7900 mass spectrometer. We follow a similar procedure to that described in González-Jiménez et al. (2021). The monitored isotopes were ^{29}Si, ^{34}S, ^{55}Mn, ^{57}Fe, ^{59}Co, ^{60}Ni, ^{65}Cu, ^{66}Zn, ^{69}Ga, ^{75}As, ^{77}Se, ^{95}Mo, ^{99}Ru, ^{100}Ru, ^{101}Ru, ^{103}Rh, ^{105}Pd, ^{106}Pd, ^{107}Ag, ^{108}Pd, ^{111}Cd, ^{115}In, ^{118}Sn, ^{121}Sb, ^{125}Te, ^{189}Os, ^{193}Ir, ^{195}Pt, ^{197}Au, ^{206}Pb, and ^{209}Bi. Laser spot sizes were set to between 33 and 55 μm. We use a laser frequency of 15 Hz, a power of 6.9 mJ/pulse and a fluence of 3 J/cm^2. An argon-helium gas mix was used as carrier gas. The ablated material was then analyzed using the mass spectrometer in time resolution mode using mass jumping and a dwell time of 10 ms/peak. Data reduction was carried out by the Iolite package for Igor Pro software (Paton et al., 2011). Count rates were normalized to the internal standard ^{57}Fe (pentlandite, pyrrhotite, awaruite), ^{61}Ni (orcelite, maucherite, nickeline) and ^{32}S (haezlewodite) using the mean values in each mineral as determined by electron microprobe. For the calibration, we use Po727 (synthetic FeS doped with approximately 40 ppm of each PGE and Au, provided by the Memorial University of Newfoundland), MASS-1 (a ZnCuFeS pressed powder pellet, doped with 50–70 ppm of most chalcophile elements and provided by the USGS), and UQAC-FeS1 (an in-house Ni-bearing FeS reference material doped with trace amounts of most chalcophile elements). The calibrations were monitored using GSE-1 g (a natural basaltic glass fused and doped with most elements at 300–500 ppm provided by USGS), UQAC-FeS5 (an in-house FeS reference material) and the own UQAC-FeS1. Analyses of these materials agreed with the certified and working values. Detection limits were calculated using background counts for the gas blank and each mineral.

In the two routines employed, Ni-rich minerals show positive correlation of Ni with Ru likely reflecting gas-related polyatomic interferences of ^{60}Ni^{40}Ar on ^{100}Ru and ^{61}Ni^{40}Ar on ^{101}Ru. Therefore measured Ru values were not considered in this study. Cadmium (^{108}Cd) interference on ^{108}Pd was corrected for using ^{111}Cd. Accuracy of the measurements on standards employed in this study is provided in Appendix 2.

4. Petrography of the Ni–Fe–S–As minerals

A total of 315 grains of Ni–Fe–S–As minerals were identified in-situ in the investigated ultramafic rocks. They consist of Ni-Fe-rich sulfides (pentlandite $(Ni,Fe)_9S_8$), smythite (Fe_9S_{11}), heazlewoodite (Ni_3S_2), millerite (NiS)), arsenides (orcelite ($Ni_{5-x}As_2$), nickeline (NiAs) and maucherite ($Ni_{11}As_8$)) and, to a lesser extent, alloys (awaruite, Ni_3Fe) and sulfarsenides (gerdorffite, NiAsS). The BMM distribute irregularly in the studied samples, as they were found only in 31 of the 150 studied polished thin-sections (Appendix 1). Sulfides are particularly abundant in the partially serpentinized massive peridotites (23 of the total 43 BMM grains identified in four samples), antigoritic massive serpentinites (83 of the total 84 BMM grains identified in one sample) and antigoritic schistose serpentinites (the 30 BMM grains identified in four samples), whereas (sulf)-arsenides are more frequent (140 of the total 150 BMM grains identified in three samples) in diopside-bearing antigorititic schistose serpentinites, and alloy (the 8 BMM grains identified in one sample) in the mylonitic serpentinites.

All sulfide grains (n = 19) identified in the partially serpentinized massive peridotites from Centinela Bajo Norte are large (up to 150 μm) euhedral grains of heazlewoodite (Hz_1) frequently associated with tiny awaruite (Aw_1;n = 5 grains) and/or magnetite (Mt_1) dispersed in the pseudomorphic lizardite mesh after olivine (Figs. 3a and 4a-g). In contrast, only one grain of Hz_1 hosting an inclusion of maucherite (Mch_1) and other three Hz_1 grains replaced by millerite (Mil_1) were found in the secondary veins of antigorite overprinting the lizardite mesh located at the margin of the F_1 folded lenses (Figs. 3b and 4h). In this microstructural setting, large grains (up to 250 μm) of orcelite (Orc_1) ± awaruite (Aw_1) ± magnetite (Mt_1) predominate (Figs. 3b and 4i-l).

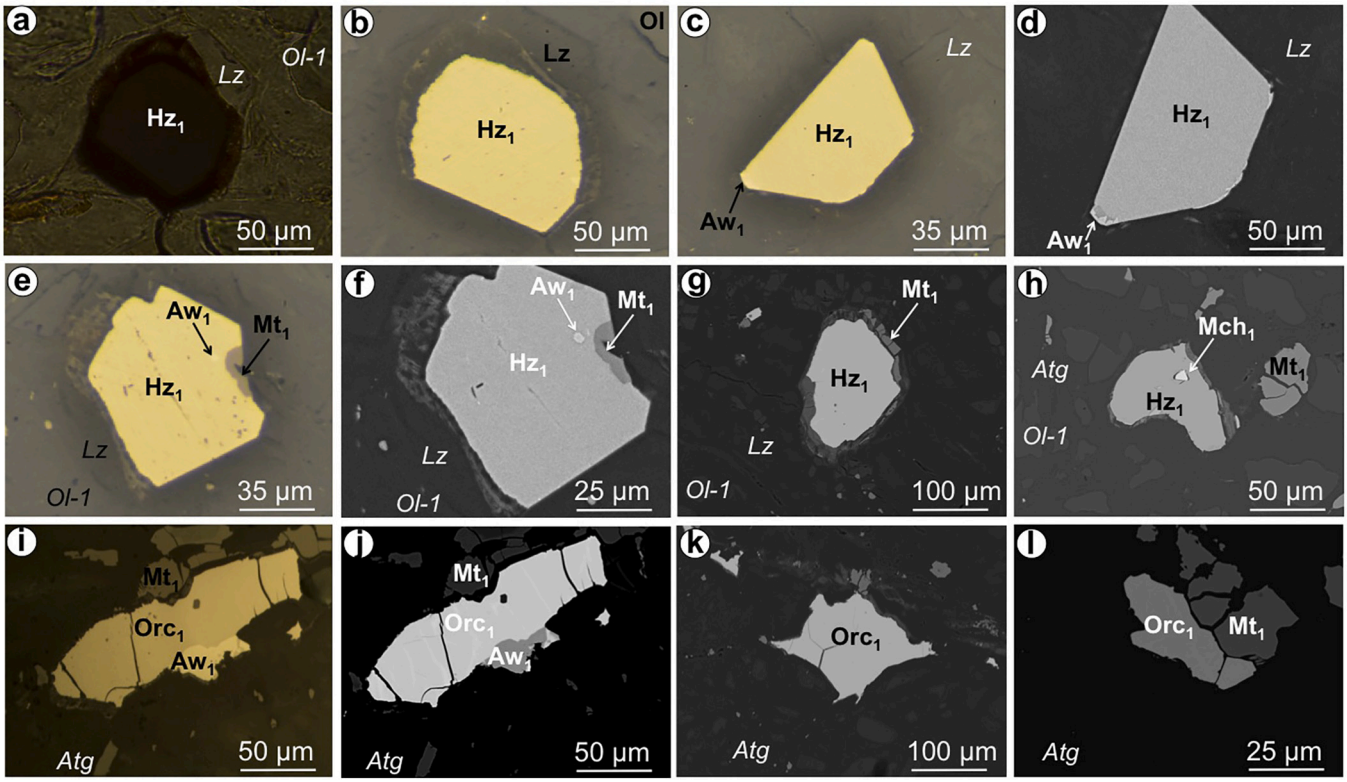

Fig. 4. Photomicrographs of representative opaque base-metal minerals in partially serpentinized massive peridotites with no deformation (a-g) and local schistosity (h-l). Images (a), (b), (c), (e) and (i) are photomicrographs under reflected light microscope (parallel nicols) whereas the remaining images are back-scattered images showing details of these pictures obtained by using FE-SEM.

Antigoritic massive serpentinites from Loma Guzmán contain a very distinct mineral assemblage dominated by large aggregates (~ 500 μm) of pentlandite (Pn_1) replaced by smythite and/or violarite ± magnetite ± pyrite (Figs. 3f and 5a-l). One of these pentlandite grains hosts a micrometric composite inclusion made up of gersdorffite and galena, whereas another pyrite includes a tiny anhedral crystal of irarsite (IrAsS) (Fig. 5g-h).

The assemblage of BMM in the antigoritic schistose serpentinites exhibiting both foliated and crenulated microstructures mainly consists of large grains (250–500 μm) of Pn_1 (25 of the 30 BMM grains identified) replaced along their rims by another generation of awaruite (Aw_2) ± magnetite (Mt_2) (Figs. 3c and 6a-f). Other composite aggregates (4 grains) comprise of Hz_1 replaced by millerite (Mil_1) (Figs. 3c and 6g-h) and a very complex grain consisting of Co-rich Pn_1 replaced by Aw_2–Mt_2 and Hz_2, in turn replaced by Mil_1 (Figs. 3c and 6i1-4). All these composite sulfide-alloy-oxide grains are oriented (and often elongated) parallel to antigorite blades defining the S_2 schistose foliation.

Diopside-bearing antigoritic schistose serpentinites contain a few (n = 10) grains of Hz_1 hosting minute inclusions of Mch_1 that are replaced by Mil_1 (Figs. 3d and 6j1-6). These rocks are singularly enriched in isolated grains (up to 300 μm across) of a second generation of orcelite (Orc_2) (120 identified from Centinela Bajo Norte body) containing antigorite blades defining the D_3 deformation, or composite intergrowths of nickeline–gersdorffite (20 grains identified from Lavanderos Body) (Figs. 3d and 6k-o). These (sulf)-arsenides are always intergrown with antigorite and diopside defining the S_3 foliation associated to F_3 folding (Figs. 3d and 6k-o).

Olivine-bearing mylonitic serpentinites only include few (n = 8) euhedral crystals (<50 μm) of a third generation of awaruite (Aw_3) dispersed within the antigorite matrix defining the S_1 foliation (Fig. 3e and 7a-d).

5. Chemistry of the Ni–Fe–S–As minerals

About 390 electron microprobe analyses and 72 single-spot laser ablation ICP-MS data were acquired in situ for Ni-Fe-S-As minerals from all the ultramafic lithotypes recognized in the La Cabaña area (Appendix 3 and 4).

5.1. Ni—Fe sulfides

Heazlewoodite EPMA analyses (n = 65) yield slightly elevated Fe contents (average 0.9 wt%) compared with the stoichiometric formula (metal (M)/sulfur (S) = 1.4–1.6; Fig. 8a). The highest Fe contents (up to 5.6 wt%) are correlated with Co (up to 6.2 wt%) in some grains of Hz_2 [$(Ni_{2.56}Co_{0.26}Fe_{0.25})_{3.07}S_{2.19}$] associated with Co-rich Pn_1 in antigoritic schistose serpentinites. The other grains yield an almost stoichiometric composition Ni_3S_2 (Appendix 3). Single-spot LA-ICP-MS analyses of Hz_1 in partially serpentinized massive peridotites (n = 5) yield higher contents of As (550–700 ppm), Co (2560–7400 ppm), Zn (2–18 ppm) and Cd (~0.76–2.80 ppm) but lower Se (~ 20–25 ppm) and Bi (<0.25 ppm) than in Hz_1 and Hz_2 grains (n = 6) from antigoritic schistose serpentinites (As ~15–357 ppm, Co ~ 320–3800 ppm, Zn < 3.5 ppm, Cd <0.08 ppm, Se ~ 23–56 ppm, Bi ~0.5–2 ppm) (Fig. 9a and Appendix 4). Grains from both lithotypes exhibit broadly similar contents of Mn (79–170 ppm), Cu (up to 64 ppm), Sb (4–20 ppm), Te (~8–17 ppm) and Pb (up to 5.5 ppm) (Fig. 9a and Appendix 4). Overall, heazlewoodites are depleted in Au and Ag (<0.06 ppm). Two grains of Hz_1 from partially serpentinized massive peridotites have noticeable amounts of Os (11 ppm), Ir (1.5 ppm), Pd (0.13 ppm) and Rh (0.02 ppm), whereas grains of Hz_2 from antigoritic schistose serpentinite are richer in Rh (2.3 ppm) and Pd (0.5 ppm) but poorer in Os (1.34 ppm) (Fig. 10a and Appendix 4). Careful inspection of the time-resolved spectra collected during LA-ICP-MS analysis support that these PGE contents are in solid solution

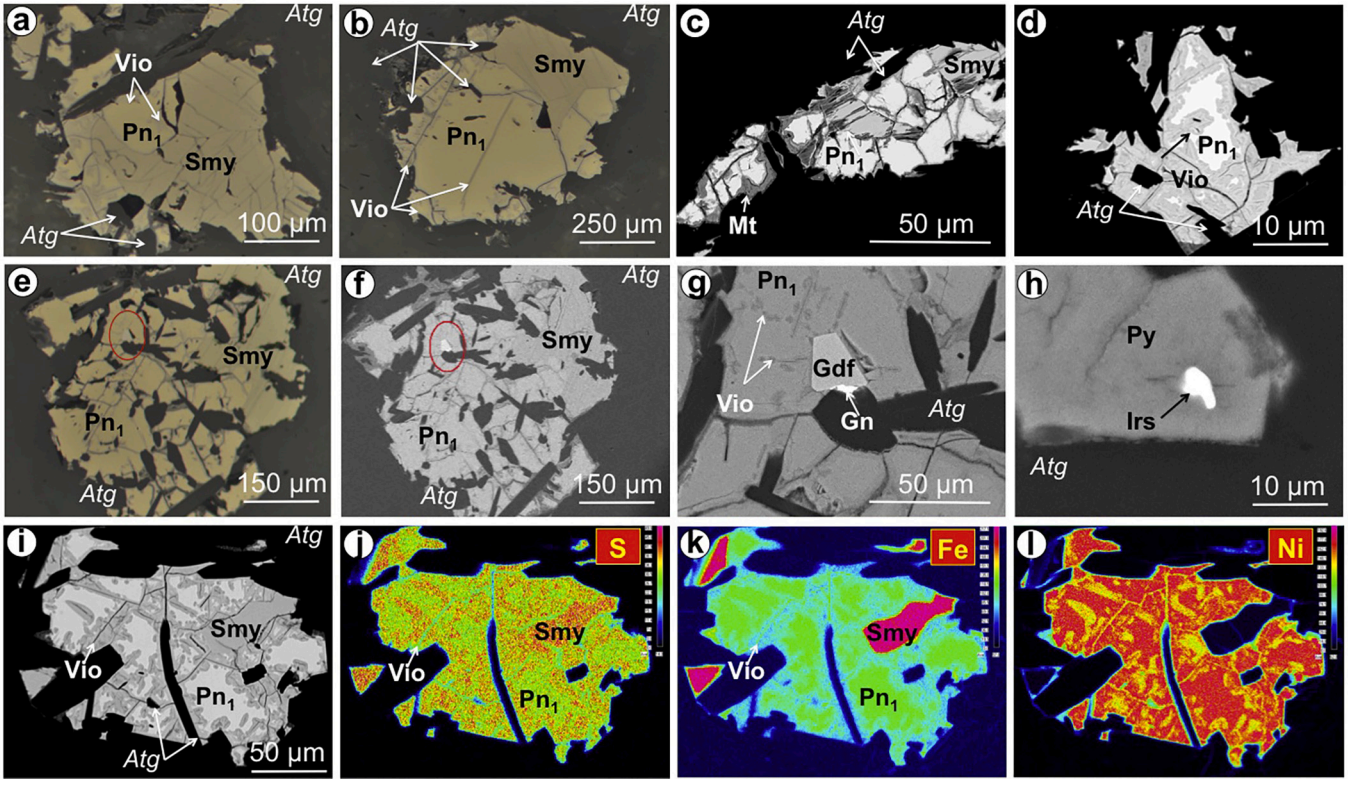

Fig. 5. Photomicrographs of representative pentlandite partially altered to smythite ± violarite ± pyrite in antigoritic massive serpentinites from Loma Guzmán. Images (a), (b), (e) are photomicrographs under reflected light microscope (parallel nicols) whereas the images (c), (d), (e), (f), (g), (h) and (i) are back-scattered images showing details of these pictures obtained by using FE-SEM. (j-i) Wavelength-dispersive spectrometry (WDS) X-ray elemental maps of the Ni—Fe sulfide assemblage shown in (i). Note that color scale bars in these maps correspond to variations in the element concentrations as counts per second.

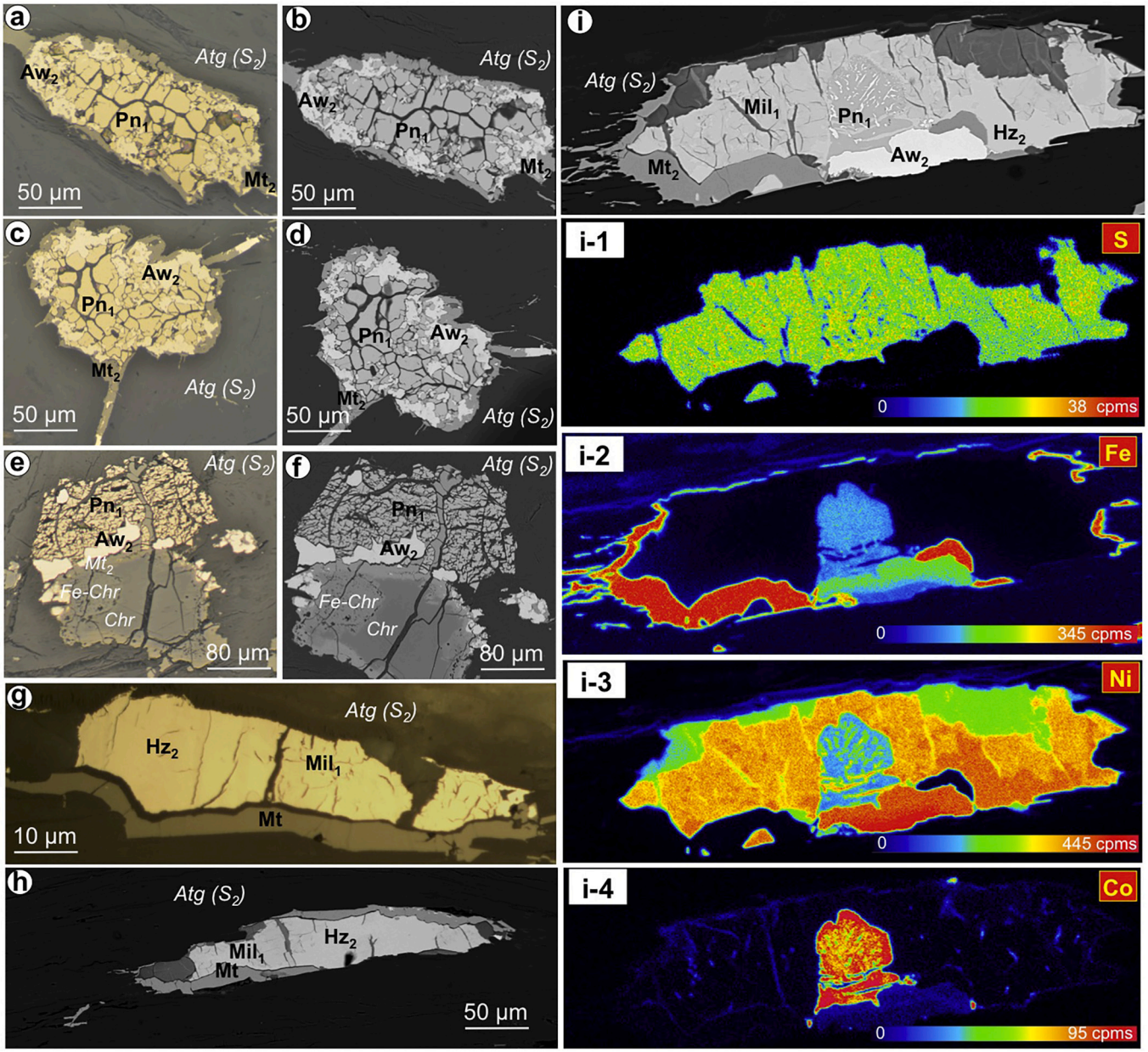

Fig. 6. Photomicrographs of representative Ni-Fe-S minerals from antigoritic schistose serpentinites (a-i) and Ni-Fe-As-S minerals from diopside-bearing antigoritic schistose serpentinites (j-o) from the La Cabaña area. Images (a-g) and (o) are photomicrographs under reflected light microscope (parallel nicols) whereas the images (h), (i), (j) and (k-n) are back-scattered images showing details of these pictures obtained by using FE-SEM. The images (i-1) to (i-4) and (j-1) to (j-6) show wavelength-dispersive spectrometry (WDS) X-ray elemental maps of the Ni—Fe sulfide-alloy assemblage shown in the images (i) and (j) respectively. Note that color scale bars in these maps correspond to variations in the element concentrations as counts per second.

within heazlewoodite.

Millerite (Mil_1) from all lithotypes has major element composition close to the ideal stoichiometry (M/S = 1.0–1.1 and average formula of $Ni_{1.04}S_{0.96}$; $n = 21$), with traces of Fe (<0.4 wt%) (Fig. 8a and Appendix 3). The LA-ICP-MS analysis of the two largest grains located in antigoritic schistose serpentinites reveal much higher contents of Co (686–1904 ppm) and As (~232 ppm) than Sb (~ 4–88 ppm), Se (55–75 ppm), Cu (2–43 ppm), Te (7–10 ppm), Pb (up to 1.8 ppm) and Bi (0.5–1 ppm) (Fig. 9b and Appendix 4). These two grains contain traces of Os (up to 0.09 ppm) whereas only one of them has detectable Rh (0.01 ppm), Pd (0.05 ppm) and Ag (0.02 ppm) (Fig. 10b and Appendix 4).

The EPMA analyses of 68 pentlandite grains show a large range in composition in the metal/sulfur ratio (M/S = 1.0–1.2; Fe/Ni_{at} = 0.4–0.9), corresponding to variable Fe (13–31 wt%), Ni (25–41 wt%) and Co (0.3–25 wt%) (Fig. 8a; Appendix 3). Grains from antigoritic massive serpentinites from Loma Guzmán (n = 34) exhibit very homogenous Co contents around 1.5 wt%, whereas a subset of grains replaced by Co-rich pentlandite from the antigoritic schistose serpentinites (n = 34) yield Co contents exceeding 10 wt% (Appendix 3). Element distribution maps show that in the latter grains Co is preferentially hosted in pentlandite and coexisting awaruite than in magnetite (Fig. 6i1-4). Thirteen pentlandites analyzed from antigoritic massive serpentinites (n = 13) yield higher contents of Bi (~4–85 ppm) and Cu (~ 23–1350 ppm) but lower As (~ 13–450 ppm), Sb (~ 1–16 ppm) and Se (~ 18–41 ppm) than six grains analyzed from antigoritic schistose serpentinites (Bi <1 ppm, Cu ~11–41 ppm, As ~38–1200 ppm, Sb ~ 2–24 ppm, Se ~ 36–76 ppm). In addition, the former pentlandites also show wider variation in Te (~ 2.4–55 ppm), Pb (~ 3–74 ppm), Zn

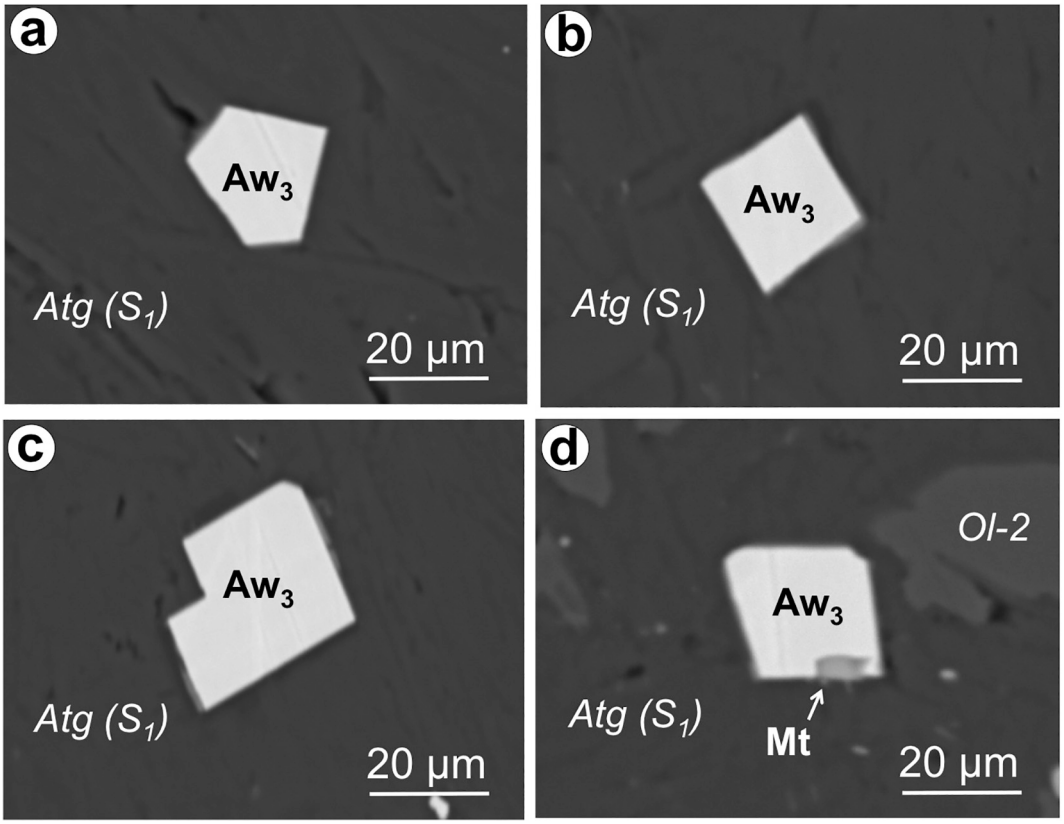

Fig. 7. (a-b) Photomicrographs taken using FE-SEM of the euhedral awaruites identified in olivine-bearing mylonitic serpentinites.

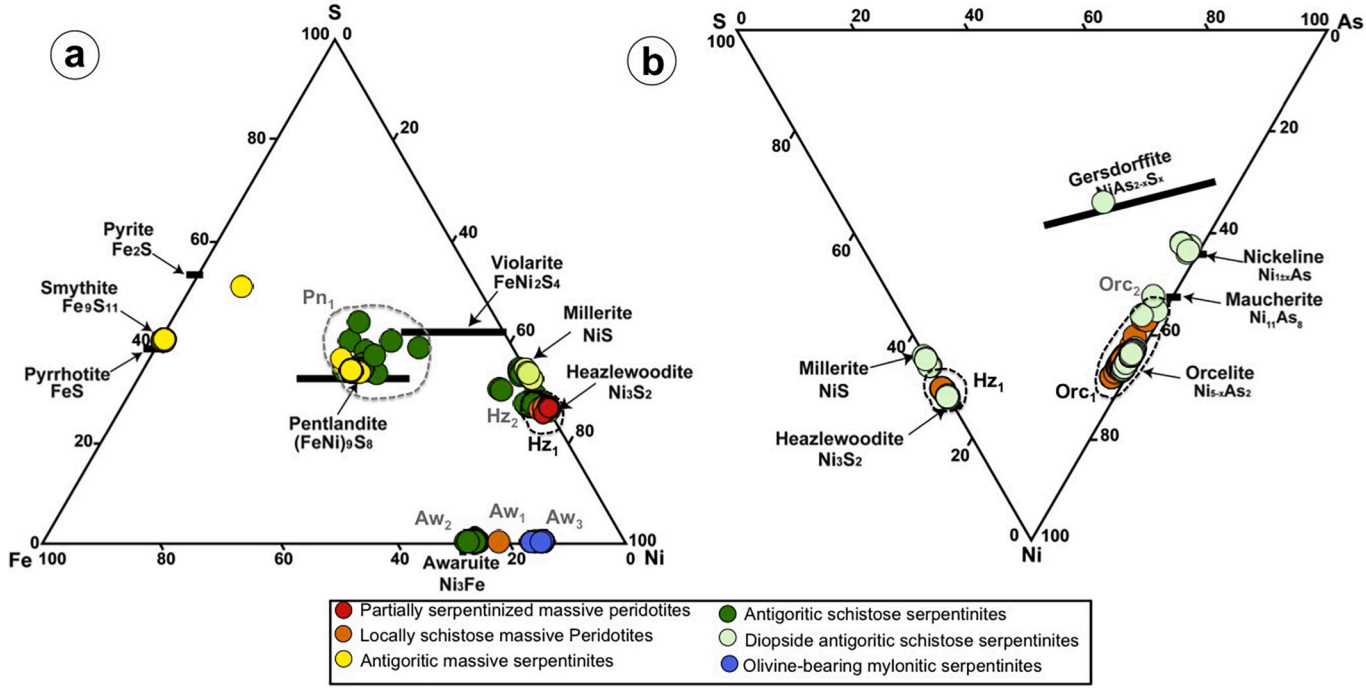

Fig. 8. Ternary plots (wt%) showing major element variations of sulfides, alloys, arsenides and sulfarsenides identified in this study in terms of Ni-Fe-S (a) and Ni-S-As (b).

(6–287 ppm) and Mn (53–800 ppm), although the Co (5800–17,400 ppm) and Cd (0.1–1.05 ppm) contents are similar in pentlandite grains from both lithotypes (Fig. 9c and Appendix 4). Most pentlandite grains from the antigoritic massive serpentinites contain traceable amounts of Ag (0.73 ppm), Au (0.69 ppm) and Pd (0.3 ppm), and in some cases Os (<1 ppm), whereas grains from antigoritic schistose serpentinites are systematically richer in Rh (~ 2–6 ppm) and Pd (0.67 ppm) but poor in Ag (<0.35 ppm), Os and Au (below detection limits) (Fig. 10c and

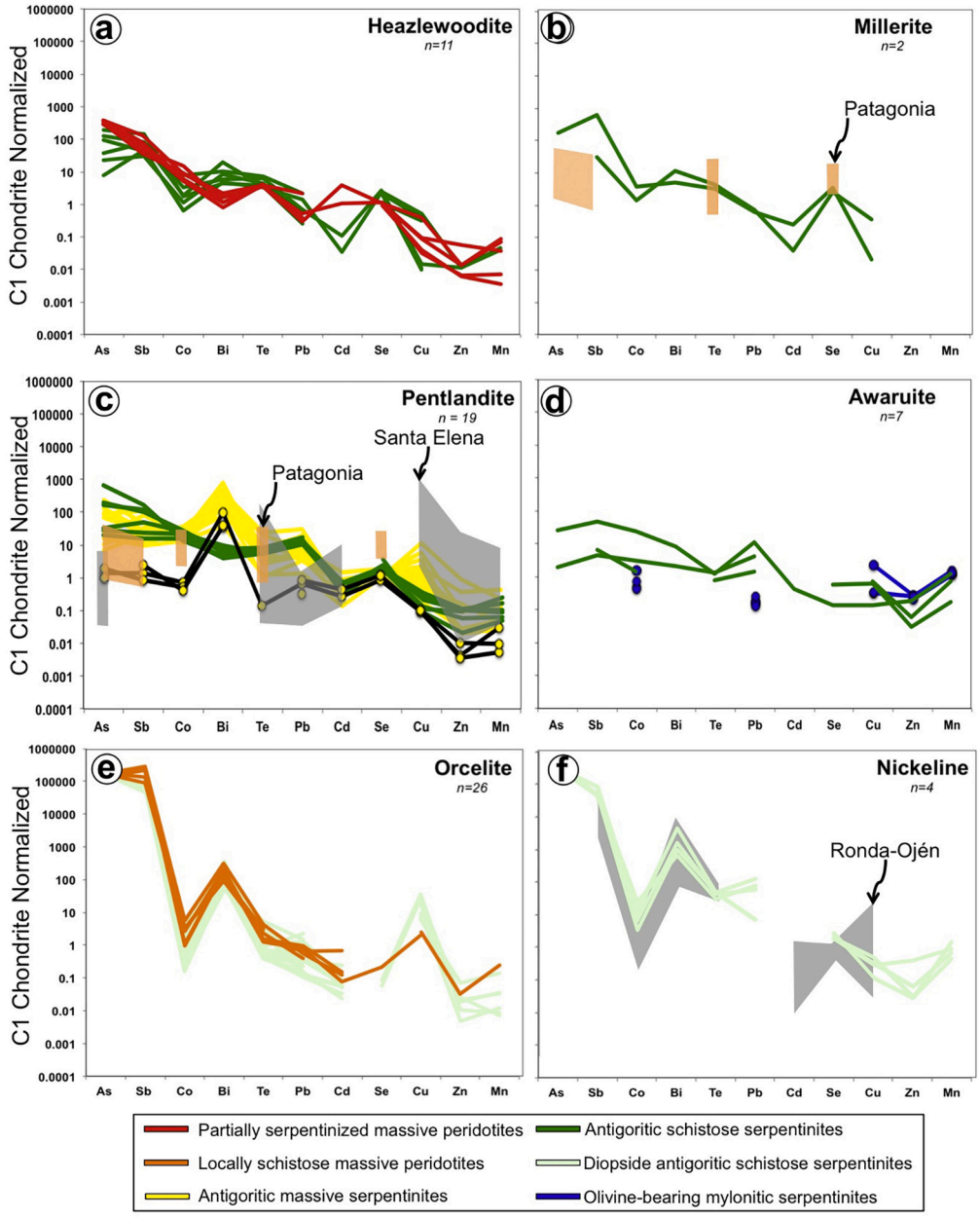

Fig. 9. Chondrite-normalized patterns of (semi)-metals (As, Sb, Co, Bi, Te, Pb, Cd, Se, Cu, Zn and Mn) of Ni-Fe-S-As minerals identified in the La Cabaña. Normalizing values from McDonough and McDonough and Sun (1995). Note that in the figure (c) yellow dots linked by solid black line correspond to smythite replacing pentlandite. Literature data plotted for comparison include: magmatic pentlandite from sub-arc mantle peridotites from the rear of the Andes in the Argentinian Patagonia (Tassara et al., 2018) and altered pentlandite from oceanic peridotites of the Santa Elena ophiolite serpentinized within the ocean floor setting (Holm, 2016). Data of magmatic nickeline from ores hosted in peridotites of the SCLM exposed in the Ronda and Ojén massif are from Piña et al. (2015). Normalizing values from McDonough and McDonough and Sun (1995). Note that in the figure (a) yellow dots linked by solid black line correspond to smythite replacing pentlandite. (For interpretation of the references to color in this figure legend, the reader is referred to the web version of this article.)

Appendix 3). Two pentlandites identified in each lithotypes contain traces of Pt (<0.2 ppm) (Fig. 10c and Appendix 4).

Smythite associated with pentlandite in the Loma Guzmán antigoritic massive serpentinites is Ni and Co-poor (<1.08 and 0.2 wt% respectively) and characterized by a rather homogenous M/S = 0.8–0.9 with a corresponding structural formula varying from $(Fe_{8.99}Ni_{0.16})_{9.15}S_{10.85}$ to $(Fe_{9.15}Ni_{0.10})_{9.25}S_{10.75}$; Appendix 3). The LA-ICP-MS analyses of three large grains yield systematically lower amounts of metals compared to pentlandite, with up to 379 ppm Co, 26 ppm Se, 12.3 ppm Cu, 11 ppm Bi, <3.7 ppm As, 3.2 ppm Zn, 2.20 ppm Pb, 0.4 ppm Sb, 0.35 ppm Te, and 0.33 ppm Cd, and precious metals <1 ppm.

Violarite replacing pentlandite in the Loma Guzmán antigoritic massive serpentinites yields very low totals of major elements, although their proportions are close to the ideal stoichiometry $FeNi_2S_4$ (M/S = 0.8–1.5; Fe/Ni_{at} = 0.5–1.2; Appendix 3). These analyses (n = 10) are here considered qualitative and yield up to 1.89 wt% Co. The other iron sulfide identified in the studied samples, i.e., pyrite, deviates from the ideal formula FeS_2 as the unique analysis carried out yields elevated amounts of Ni (up to 8.82 wt%) and Co (1.71 wt%) due to fluorescence effects from the nearby Co-rich pentlandite (Fig. 8a and Appendix 3).

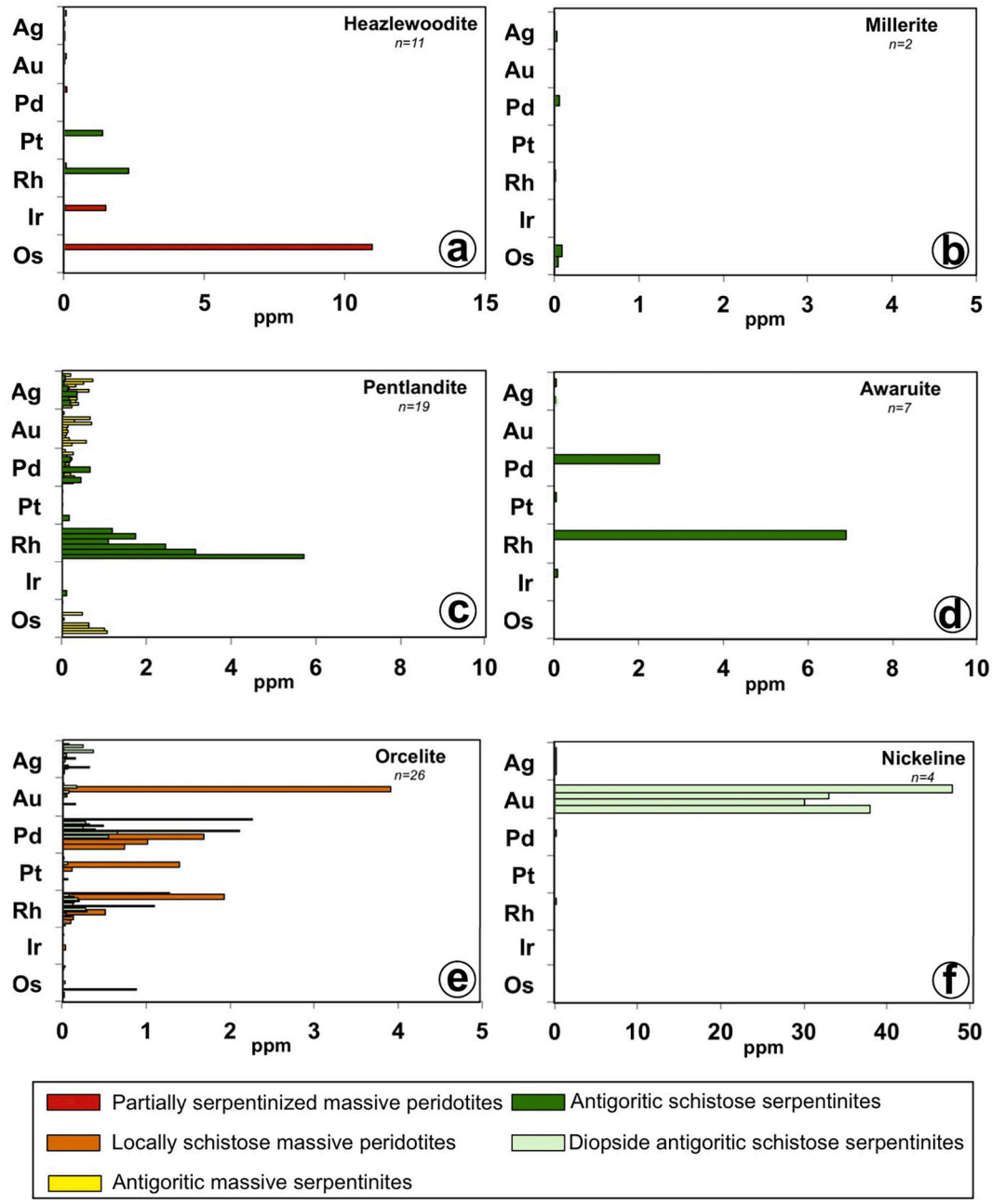

Fig. 10. Concentrations of precious metals (ppm) measured in (Ni—Fe)-bearing sulfides (a-c), Ni—Fe alloy (d) and (sulf)-arsenides (e-f) in the studied serpentinites from La Cabaña área.

5.2. *Ni—Fe alloys*

All the Ni—Fe alloys analyzed from La Cabaña serpentinites ($n = 52$) are awaruite (Ni_2Fe to Ni_3Fe), with chemistry falling into three compositional groups roughly related to the host serpentinite lithotype (Fig. 8a and Appendix 3).

The awaruite (Aw_1) associated with Orc_1 and/or Mt_1 in the locally schistose partially serpentinized massive peridotites ($n = 3$) has Fe/Ni_{at} = 0.2–0.3, corresponding to high Ni (76–81 wt%; $Ni_{2.51}Fe_{0.49}$ to $Ni_{3.14}Fe_{0.86}$), Cu (1.8 wt%), As (0.8 wt%) and low Co (0.75 wt%) (Fig. 8a and Appendix 3).

In contrast, Aw_2 replacing Pn_1 in the antigoritic schistose serpentinites ($n = 30$) yield Fe/Ni_{at} = 0.3–0.4, corresponding to the lowest Ni (71–75 wt%; $Ni_{2.89}Fe_{1.11}$ to $Ni_{2.98}Fe_{1.02}$) and highest Co contents (up to 3.7 wt%) with negligible traces of As (0.5 wt%), Cu (0.2 wt%), and S (0.1 wt%) (Fig. 8a and Appendix 3). Consistently, more precise single-spot LA-ICP-MS analysis of the three largest of these Aw_2 grains yield Co <13,200 ppm, and very low contents of As (<49 ppm) and Cu (<95 ppm). The other (semi)-metals are present even in lower concentrations with Pb <30 ppm, Se < 13 ppm, Sb <7 ppm, Te < 3.35 ppm, Bi <1 ppm, Cd < 0.32 ppm (Fig. 9d and Appendix 4). Two of the analyzed grains contain detectable amounts of Ag (~ 0.06 ppm) whereas one of them is enriched in Rh (6.9 ppm) and Pd (2.48 ppm) and also host traces of Ir (0.07 ppm) and Pt (0.04 ppm) (Fig. 10d). The other precious metals are below their detection limits.

The third generation of awaruites (Aw_3) found as isolated grains in the olivine-bearing mylonitic serpentinites ($n = 19$) exhibits the most homogenous (Fe/Ni_{at} = 0.2) and nickel-rich composition (Ni = 80–83 wt%; $Ni_{2.47}Fe_{0.53}$ to $Ni_{2.55}Fe_{0.45}$) with the lowest Co contents (0.5 wt%) and negligible As and S (Fig. 8a and Appendix 3). Consistently, LA-ICP-

MS analyses of four of these grains reveal very low Co (<750 ppm) and As below detection limit. Other analyzed (semi)-metals and all precious metals are also below detection limits, excepting Mn (2160–2940 ppm), Cu (37–270 ppm), Zn (63–83 ppm) and Pb (0.3–0.6 ppm) (Fig. 9d and Appendix 4).

5.3. Ni arsenides and sulfarsenides

Orcelite (n = 135) has a large compositional range in terms of As (27.6–37 wt%), Ni (7.98–51.56 wt%) and Sb (0.6–11 wt%) and Co consistently below 1.93 wt% (Fig. 8b and Appendix 3). The largest variations in all these elements were detected in Orc_1 found as isolated grains or grains associated with Aw_1 and/or Mt_1 in locally schistose partially serpentinized massive peridotites [$Ni_{1.49}(As_{1.66}Sb_{0.30}Fe_{0.04})_2$ to $Ni_{2.76}(As_{1.79}Sb_{0.16}Fe_{0.04}Co_{0.01})_2$; n = 45], which also show Sb contents >1.5 wt% (Appendix 3). The LA-ICP-MS analysis of six Orc_1 grains from this lithotype confirms their enrichment in Sb (12,800–39,043 ppm) relative to Co (465–2744), and noticeable concentrations of Cu (242–2700 ppm), the latter within the range previously detected by EPMA (<0.62 wt%) (Fig. 9e and Appendix 4). These orcelite grains also contain hundreds ppm of Mn (up to 480) but low abundances of Bi (<11–35 ppm), Te (3–10 ppm), Zn (<10 ppm), Se (<0.5 ppm), Cd (<0.5 ppm) and Pb (<2.3 ppm). They also host in solid solution Au (~ 4 ppm), Rh (~2 ppm), Pd (<1.6 ppm) and Ag (<0.07 ppm), but only few grains have traceable Pt (<1.4 ppm), Ir (<0.034) and Os (<0.020) (Fig. 10e and Appendix 3).

The second generation of orcelite grains (Orc_2) found in the diopside-bearing antigoritic schistose serpentinites have more homogenous EPMA compositions [$Ni_{2.16}(As_{1.81}Sb_{0.03}Fe_{0.15})_2$ to $Ni_{2.66}(As_{1.97}Sb_{0.03}Fe_{0.01})_2$; n = 90] and Sb <1.22 wt% (Fig. 8b and Appendix 3). In situ LA-ICP-MS analysis of twenty of these grains confirms these lower Sb (6252–10,400 ppm) and Co (80–2280 ppm) contents than in orcelite from locally schistose partially serpentinized massive peridotites (Fig. 9e and Appendix 4). This type of orcelites also exhibits higher Cu (244–5481 ppm) and Pb contents (up to 5.8 ppm), lower concentrations of Mn (<268 ppm), Se (<2 ppm) and Cd (<0.2 ppm) and more variable Bi (6–41 ppm), Te (1–13 ppm) and Zn (~ 2–22 ppm) (Fig. 9e and Appendix 4). Most of the analyzed grains also contain Au, Ag, Rh, and Pt in much lower amounts (Au <0.16 ppm, Rh <1.3 ppm, and Pt <0.06 ppm) and much abundant Pd (up to 2.26 ppm) and Os (up to 0.88 ppm) than orcelite in locally schistose partially serpentinized massive peridotites (Fig. 10e and Appendix 4).

The three analyzed grains of Mch_1 found in the diopside-bearing antigoritic schistose serpentinites are very rich in Sb (~ 8.5 wt% on average; n = 3) (Appendix 3). The average structural formula for these three grains is $(Ni_{11.15}Fe_{0.20})_{11.35}(As_{6.74}Sb_{0.91})_{7.65}$ (Fig. 8b). Because of their small size, these grains were not amenable for reliable in situ LA-ICP-MS analysis.

Nickeline in diopside-bearing antigoritic schistose serpentinites has a very homogenous composition with a structural formula varying from $(Ni_{0.99}Fe_{0.01})_1(As_{0.99}Sb_{0.01})_1$ to $(Ni_{1.02}Fe_{0.01})_{1.02}(As_{0.97}Sb_{0.01})_{0.98}$ (n = 10) (Fig. 8b and Appendix 3). The Sb and Co contents detected by by LA-ICP-MS yield up to 11,400 ppm Sb and 11,900 ppm Co (Fig. 9f and Appendix 4). These grains analyzed by LA-ICP-MS yield Cd contents below detection limits but noticeable amounts of Mn (860–2830 ppm), Bi (70–470 ppm), Pb (17–310 ppm) and, to lesser extent, Zn (90–120 ppm), Te (69–111 ppm), Se (36–57 ppm) and Cu (14–57 ppm) (Appendix 4). All these grains also show conspicuous amounts of Au (up to 48 ppm) and Ag (up to 0.3 ppm), but they are depleted in PGE with only traces of Rh (0.031 ppm) and Pd (0.071) detected in two of the analyzed grains (Fig. 10f and Appendix 4).

EPMA, but not LA-ICP-MS, analysis was possible only in one grain of gersdorffite (Fig. 8a and Appendix 3), yielding the following structural formula: $(Ni_{0.98}Co_{0.21}Fe_{0.01})_1(As_{0.99}Sb_{0.01})_1S_1$.

6. Discussion

6.1. Genesis of the Ni–Fe–S–As minerals

6.1.1. The assemblage heazlewoodite–awaruite–magnetite linked to lizarditization of mantle wedge serpentinites

Euhedral grains of heazlewoodite (Hz_1) are the most common BMM in partially serpentinized massive peridotites. They are exclusively found in lizardite mesh (Figs. 3a and 4a-g), suggesting they could form from Ni released during static serpentinization of olivine (or pyroxene) at ≤300 °C by the following reaction (Eq. 1 after Song et al., 1995):

$$3NiO_{(in\ silicate)} + S_{2(aq)} \rightarrow Ni_3S_2 + 3/2\ O_2 \quad (1)$$

The association of awaruite (Aw_1) and/or magnetite (Mt_1) with some of these heazlewoodite grains (e.g., Fig. 4c-f) reflects that metal loss from silicates was not only balanced by the formation of heazlewoodite. In particular, Ni and Fe available in the system after formation of Hz_1 may have parted to form both Aw_1 and Mt_1 (Arai et al., 2020; Filippidis, 1985; Frost, 1985). Alternatively, the minute inclusions of Aw_1–Mt_1 in Hz_1 (e.g., Fig. 4e-f) could reflect replacement of pre-existing Ni—Fe alloy–oxides assemblages. Theoretical calculation (Frost, 1985; Klein and Bach, 2009; Schwarzenbach et al., 2014) and empirical results (Beard and Hopkinson, 2000; Eckstrand, 1975) in the Fe-Ni-Co-O-H-S-Mg-Si system indicate that oxidation of Fe from olivine and/or pyroxene during serpentinization produces magnetite and significant amounts of H_2. This results in an environment with very low fO_2 and fS_2 (Evans et al., 2017; Frost, 1985; Klein and Bach, 2009) where Ni-rich S-poor sulfides and alloy may coexist with magnetite. Considering the P-T conditions estimated for the initial hydration of the investigated rocks (≤ 300 °C and < 1 GPa), the assemblage $Hz_1 \pm Aw_1 \pm Mt_1$ could form in equilibrium with lizardite at log fO_2 ~ −40 to −38 and log fS_2 < −19 (point 1 in Fig. 11a).

The two mechanisms proposed for the formation of Hz_1 required Ni in olivine from the ultramafic protolith, as well as S (either from the protolith or from an external aqueous fluid source). The olivine of partially serpentinized massive peridotites from originally dunites and harzburgites is relatively rich in NiO (up to 0.45 wt%; González-Jiménez et al., 2014; Plissart et al., 2019), as common primary olivine in mantle peridotites. Moreover, partially serpentinized massive peridotites have relatively high concentrations of fluid mobile elements (e.g., As, Sb, Pb, Cs and Li) similar to other lizardite serpentinites originated in mantle wedges (González-Jiménez et al., 2016), supporting that infiltration of slab fluids also supplied S to the rocks (Fig. 12; e.g., Alt and Shanks, 2003; Debret et al., 2014). The high Se content in the analyzed heazlewoodites (up to 56 ppm) is also consistent with their precipitation from slab-derived fluids (Hattori et al., 2002).

6.1.2. Precipitation of pentlandite and Ni-rich (sulf)-arsenides at the beginnings of antigoritization

The infiltration of subduction-related fluids carrying S, As, and Pb during serpentinization is also corroborated by the presence of gersdorffite and galena associated with As-and Sb-rich Pn_1 intergrown with antigorite in antigoritic massive serpentinites (Fig. 5e-g). These microstructural relationships suggest that all these minerals precipitated shortly before, or contemporarily to, infiltration of fluids that produced the static antigoritization predating the D_1 deformation phase (Fig. 12). Filippidis (1982) carried hydration experiments of olivine in the presence of S at 350 °C and 0.2 GPa, reporting the formation of pentlandite at log fO_2 and log fS_2 values greater than −38 and − 17, respectively. Recent observation on subducted serpentinites from the Zermatt Saas ophiolite (Evans et al., 2017; Piccoli et al., 2019) and Alpine Corsica (Crossley et al., 2020) confirmed these experiments, reporting the formation of pentlandite during prograde antigoritization. Phase equilibria diagrams for subducted serpentinites in the systems Fe–Ni–O–H–S and Fe–Ni–O–S by Evans et al. (2017) suggest that pentlandite is stable at the

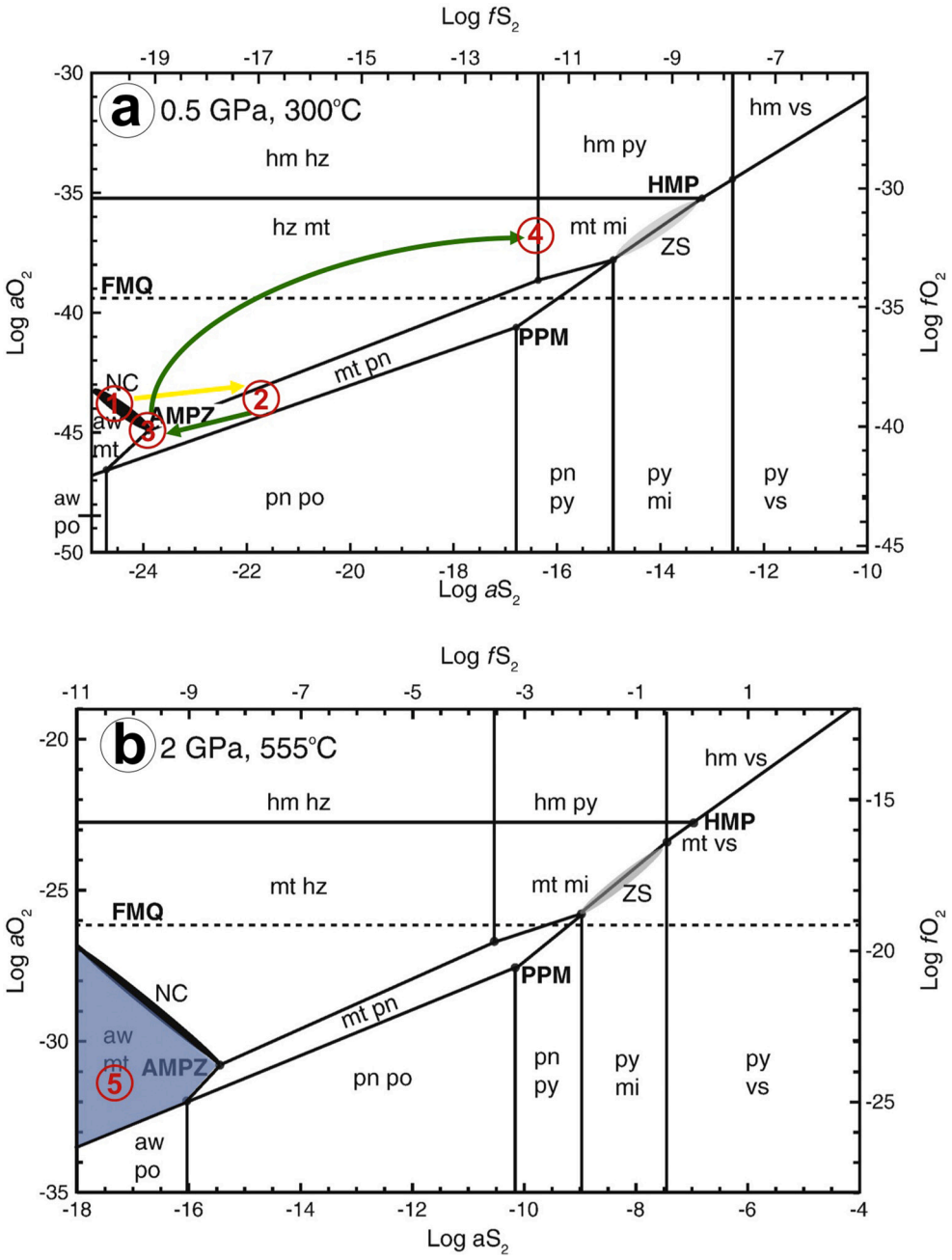

Fig. 11. (a) Phase relations in the system Fe–Ni–O–S expressed in activity-activity aO_2–aS_2 diagram and corresponding fO_2–fS_2 at 300 °C and 0.5 PGa, and at 550 °C and 2 GP after Evans et al. (2017). The numbered dots and arrows indicate indicate the evolution of the mineral assemblages in the samples of La Cabaña invetigated here throughout the entire subduction cycle.

minimum fO_2-fS_2 conditions determined from the experiments at 300 °C and 0.5 GPa (point 2 in Fig. 11a). The temperatures of formation of static antigorite in the investigated rocks overlap the thermal range of the aforementioned experimental and modeling works. If these latter experiments carried out at low pressure could be extrapolated to serpentinites subducted to higher pressure, then formation of these metallic minerals should have been taking place as a result of an increasing of fO_2 and fS_2 by infiltration of progressively hotter fluids during antigoritization (yellow path 1 ⇒ 2 in Fig. 11a). Noteworthy, in the cited works, pentlandite was observed in equilibrium with magnetite ± heazlewoodite with or without awaruite. The higher variance assemblage (pentlandite + magnetite) observed here does not permit to constrain the values of fO_2 and fS_2 during the prograde fluid infiltrating process (the assemblage is divariant at isothermal-isobaric conditions, Fig. 11a) although the range in fO_2 is rather restricted for a given fS_2, with a minimum value constrained by the absence of pyrrhotite. The temperature estimated applying the Co content in Pn_1 from antigoritic massive serpentinites ($T \leq 200$ °C, Fig. 13a) clearly contrasts with the temperature of formation of the pentlandite estimated from experiments and comparison with other natural high-pressure serpentinites. Most likely, these temperatures reflect the latest stages of alteration of Pn_1 once serpentinites were already exhumed (see section 6.3) rather than crystallization temperature during the prograde path.

A grain of Hz_1 hosting an inclusion of Mch_1 was also found in antigorite from the locally schistose part at the margins of F_1 folds affecting massive serpentinites (Fig. 4h). In this lithotype, the assemblage of BMM is dominated by Sb-rich Orc_1 ± Aw_1 ± Mt_1 (Fig. 4i-l). The exclusive presence of these Ni-arsenides in the prograde veins of antigorite

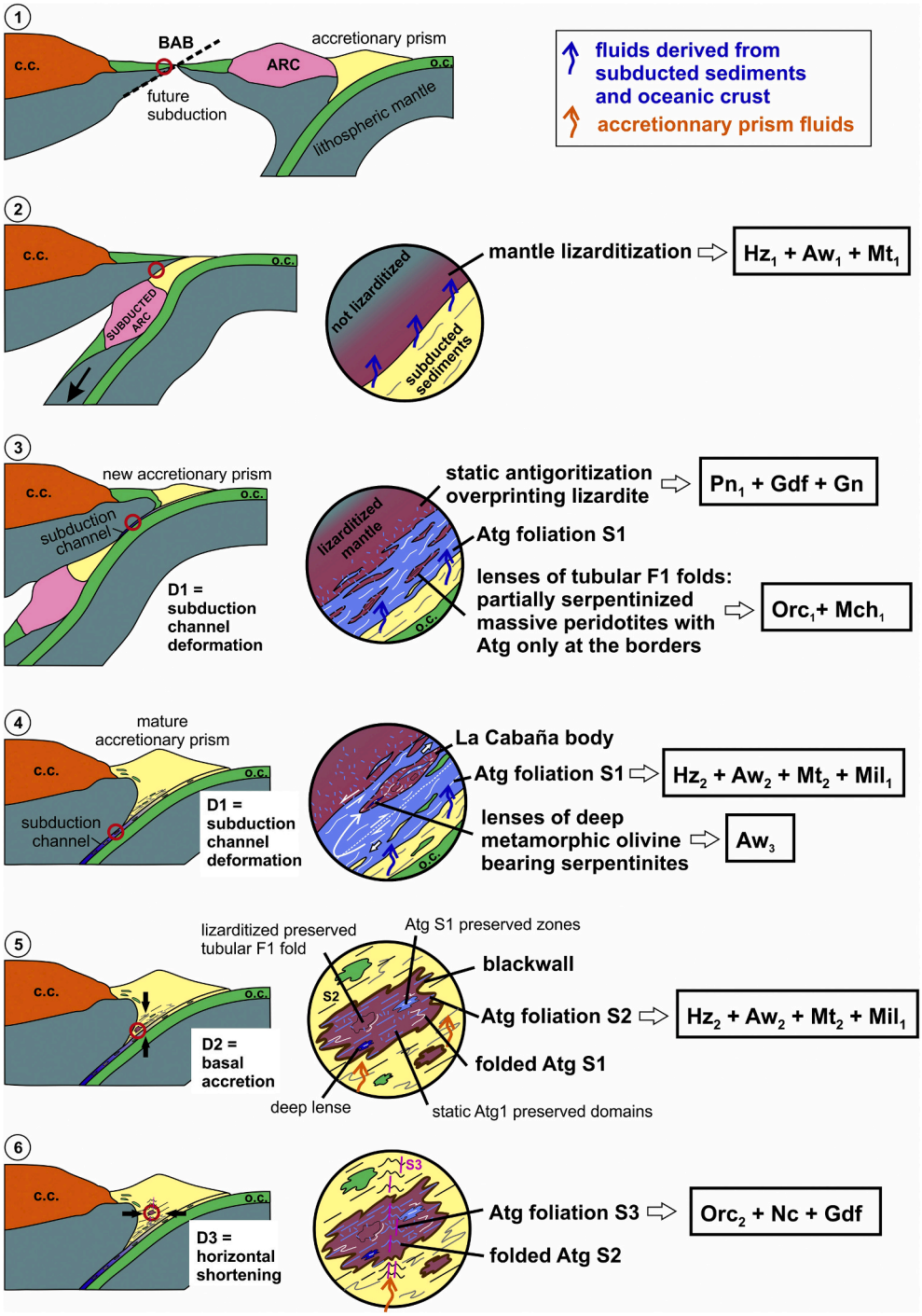

Fig. 12. Schematic cross-section showing the tectonic configuration of the Palaeozoic subduction zone in south-central Chile and the proposed model for the origin of the studied rocks and their related BMM. The sketch is an adaptation from Plissart et al. (2019).

defining the nascent S_1 foliation suggests their formation shortly before or at the very early beginnings of the D_1 deformation, when mantle wedge lizardite peridotites were being incorporated into the subduction channel (Fig. 12; Plissart et al., 2019). Phase relations in the Ni–As–S system have not been established yet at high pressures, however experimental data obtained by Yund (1962) in low pressure experiments for this system indicate that the assemblage $Ni_{3\pm x}S_2$–maucherite is stable above 556–524 °C, while from these temperatures to below 450 °C heazlewoodite–maucherite is the stable assemblage. In the cited experiments, the assemblage maucherite–$Ni_{3\pm x}S_2$ was produced by the reaction of pre-existing heazlewoodite with As-S-rich fluids. In the investigated rocks, Orc_1 replace Aw_1 and Mt_1 (Fig. 4i-j), supporting the reaction of pre-existing Ni-rich sulfide-oxides with incoming As-rich fluids. Thus, we suggest that Hz_1 formed during early stages of lizarditization interacted with hotter As- and S-bearing fluids during antigoritization, producing assemblages of $Ni_{3\pm x}S_2$–maucherite, which further re-equilibrated below 450 °C into the Hz_1–Mch_1 (Fig. 4h). The temperatures estimated for the formation/equilibration of the assemblage Hz_1–Mch_1 are only marginally higher than those of formation of prograde antigorite (~320–400 °C; Plissart et al., 2019). Moreover, they overlap those calculated for the metamorphic alteration of chromites in chromitites from Lavanderos (~560–430 °C; González-Jiménez et al.,

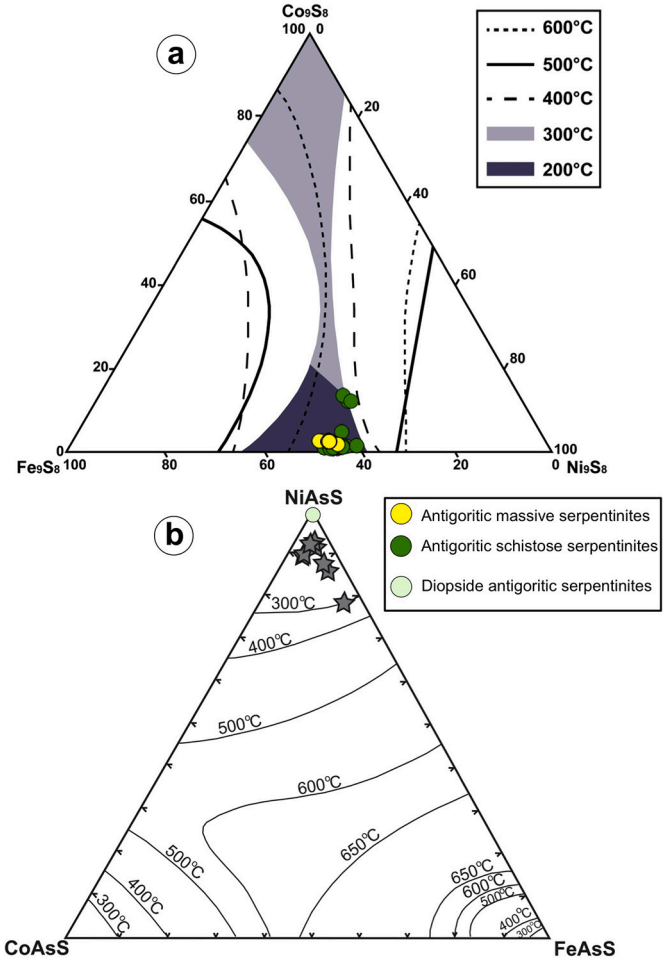

Fig. 13. (a) Chemistry of pentlandite in terms of the ternary system Fe_9S_8–Ni_9S_8–Co_9S_8, showing the temperature-dependent stability fields for the formation of pentlandite (after Kaneda et al., 1986). Pentlandite hosted in schistose antigoritic serpentinites and antigoritic massive serpentinite occupies a narrow range in composition at 300–200 °C. Note that a few pentlandite grains with anomalously high Co content (>10 wt%) as those shown in Fig. 6i were not plotted in this diagram. (b) Plot of the analyzed gersdorffite grain with references of the solvus in the condensed system CoAsS–NiAsS–FeAsS at 300 °C, 400 °C, 500 °C, 600 °C, and 650 °C (Klem, 1965). Note that grey stars correspond to previous data of nickeline found in metamorphic rims of chromite and antigoritic matrix of chromitites hosted in the same diopside-bearing white-soap schistose serpentinites by González-Jiménez et al. (2016). Legend is inset in the figures.

2016), suggesting local infiltration of hotter fluids through discrete zones of the developing F_1 folds (Fig. 12).

All the observations above suggest that certain volumes of As- and Sb-bearing fluids already infiltrated the olivine–lizardite peridotites before the development of S_1 and continued during antigoritization (Fig. 12). Consistently, bulk-rock compositions indicate that locally schistose partially serpentinized massive serpentinites are enriched in As and Sb relative to the olivine–lizardite dunites (González-Jiménez et al., 2016). Stable chlorine isotope data (Barra et al., 2012) fingerprint a sedimentary source for these fluids producing antigoritization, which could be derived from meta-sediments dehydrating within the serpentinitic subduction channel (González-Jiménez et al., 2016; Plissart et al., 2019).

6.1.3. Modification of Ni—Fe sulfides within the shallow portion of the serpentinitic subduction channel and at the base of the accretionary prism

Experimental and natural observations indicate that the assemblages of pentlandite–heazlewoodite–awaruite–magnetite may form in equilibrium with serpentine when peridotite is hydrated at low fO_2 and fS_2. We have identified composite aggregates of Co-rich pentlandite ± heazlewoodite ± awaruite ± magnetite in antigoritic schistose serpentinites (Figs. 3c and 6a-i). However, mineral paragenesis and microstructures suggest that earlier pentlandite (Pn_1) was replaced by heazlewoodite ± awaruite ± magnetite. Significant amounts of H_2 may be available in the system until olivine is completely exhausted in the rock (Vitale Brovarone et al., 2020). In this environment, S-rich sulfides tend to equilibrate with the H_2-rich fluids and form S-poorer sulfides alloys (Eckstrand, 1975; Evans et al., 2017; Frost, 1985; Klein and Bach, 2009). Antigoritic schistose serpentinites locally contain ribbons of relic lizardite-olivine, suggesting the possible equilibration of early-formed Pn_1 with H_2-rich fluids produced during local antigoritization of relic olivine. For example, the replacement of Pn_1 by awaruite (Aw_2)–magnetite (Mt_2) observed in Fig. 6a-f can be described by the following reactions (Eq. 2, after Klein and Bach, 2009):

$$Ni_{4.5}Fe_{4.5}S_8 + 4H_2(aq) + 4H_2O \rightarrow 3Ni_3Fe + 2Fe_3O_4 + 16H_2S(aq) \quad (2)$$

Further reaction of Aw_2 with H_2S from fluids may result in the formation of a second generation of heazlewoodite (i.e., Hz_2 in Fig. 6i) as follows (Eq. 3, after Klein and Bach, 2009):

$$3Ni_3Fe + 6H_2S(aq) + 4H_2O \rightarrow Ni_3S_2 + Fe_3O_4 + 10H_2(aq) \quad (3)$$

A maximum temperature of ~300–400 °C is suggested for the equilibration of altered Pn_1 from antigoritic schistose serpentinites based on its Co content (Fig. 13a; Kaneda et al., 1986). These temperatures overlap thermal range estimated for antigoritization (320–400 °C) within the serpentinitic subduction channel, thus suggesting that if these experiments carried out at ambient pressure can be extrapolated to the given pressures (< 1.0 GPa). A local shifting towards lower fugacities of oxygen ($\log fO_2 \sim -40$) and sulfur ($\log fS_2 \sim -19$) promoted reactions (2) and (3) in the investigated rocks (green path 2 ⇒ 3 in Fig. 11a).

Some grains of Hz_1 and Hz_2 are partially replaced by millerite (Mil_1) in the antigorite matrix of antigoritic schistose serpentinites (Figs. 3b-c and 6g-i). This texture of disequilibrium may be explained by the following reaction (Klein and Bach, 2009):

$$Ni_3S_2 + H_2S(aq) \rightarrow H_2(aq) + 3NiS \quad (4)$$

This reaction implies a substantial increasing of fO_2 and fS_2 to values above the quartz–fayalite–magnetite (QFM) buffer. According to the phase relations constructed by Evans et al. (2017), this reaction occurs at a minimum value of $\log fS_2 \sim -11.5$ and a range in $\log fO_2$ from ~ −34 to −30 (green path 3 ⇒ 4 in Fig. 11a). Considering that the minimum fO_2 and fS_2 were reached when primary igneous olivine was still present and that H_2 production stopped when olivine was locally exhausted in some of these rocks (Frost, 1985), such increase in both fO_2 and fS_2 could be related with the complete serpentinization similar to other serpentinites that have experienced subduction zone metamorphism (e.g., Evans et al., 2017). The observation that these millerite-bearing grains are oriented parallel to S_2 foliation suggests that the fO_2 and fS_2 shifted to higher values before, or at least contemporarily to, the D_2 deformation phase registering the incorporation of the subducted serpentinites into the accretionary prism (Fig. 12). As noted above, this D_2 deformation phase was a subvertical shortening also recorded in enclosing micaschists that took place at ~280 Ma ago (Romero et al., 2018).

6.1.4. Modification of Ni—Fe sulfides within the deep serpentinitic subduction channel

As noted above, olivine-bearing mylonitic serpentinites record the highest metamorphic conditions as a result of their burial towards the deepest portions of the subduction channel (Fig. 12). These rocks only contain a few grains of Aw_3 (Figs. 3e and 7a-d) with a rather homogenous and higher Ni contents as well as a very distinct distribution of

(semi)-metals than Aw_1 and Aw_2 (Fig. 9d; Appendix 1 and 2). The well-developed habit of this Aw_3 suggests equilibrium with the assemblage antigorite-metamorphic olivine formed during prograde metamorphism of serpentinites within the subduction channel. Thermodynamic calculations in the Fe–Ni–O–H–S–Mg–Si system at P-T conditions (300–555 °C and 0.5-2GPa; Foustoukos et al., 2015; Evans et al., 2017) indicate that the field of stability of awaruite significantly enlarge towards higher fO_2 and fS_2 values upon increasing P-T conditions of metamorphism (Fig. 11a-b). Likewise, these results indicate that assemblages of awaruite (± magnetite) (Fig. 7a-d) could form at increasing pressures by S loss with/without necessity of decreasing in fO_2 (point 5 within blue field in Fig. 11b). Considering that olivine-bearing mylonitic serpentinites register peak metamorphic conditions at ~600 °C and 1.1 GPa (Plissart et al., 2019) compatible with subduction, the formation of Aw_3 during dehydration could therefore be interpreted to register the uptake of Ni from pre-existing Ni-rich sulfides/arsenides or serpentine.

6.1.5. Stability of Ni–Fe–S–As minerals during exhumation and retrogression within the accretionary prism

Diopside-bearing antigoritic schistose serpentinites well register the final exhumation of the La Cabaña serpentinites in the accretionary prism. (Fig. 12) This type of serpentinites, which originated during the D_3 deformation phase, contains Hz_1 hosting inclusions of Mch_1 that is replaced by Mil_1 (Fig. 6j1-6). Mil_1 formed before or contemporarily to the D_2 deformation phase, suggesting that this heazlewoodite–maucherite–millerite assemblage is relict.

However, the most striking characteristic of the diopside-bearing antigoritic schistose serpentinites is their singular enrichment in Ni-rich arsenides and sulfarsenides relative to the other serpentinites of La Cabaña area. Their mineral assemblages include a second generation of orcelite (Orc_2) overgrowing magnetite (Fig. 6k-n) and/or composite aggregates of nickeline-gersdorffite (Fig. 6o), all of them protruded or intergrown with antigorite (and diopside) defining the S_3 foliation (Fig. 3d). The observation that orcelite from diopside-free and diopside-bearing antigoritic schistose serpentinites exhibit almost identical distributions of (semi)-metals and precious metals (Fig. 9e and 10e) suggests that discrete domains of schistose antigoritic serpentinites already contained this mineral before the F_3 folding. However, a careful inspection of antigoritic schistose serpentinites reveals that these rocks lack As-rich minerals. This observation suggests that fluids with the higher amounts of As and Sb were preferentially channelized in zones of focused strain upon antigoritization. Thus, the exclusive location of Orc_2 in the hinges of the S_3 crenulation and the fact that they are protruded to or contain antigorite blades defining the D_3 deformation (e.g., Fig. 6k-n) suggest that zones that accumulated higher strain while precipitating Ni-rich arsenides were later reactivated during exhumation, producing recrystallization of the pre-existing Orc_1 to Orc_2. Above (section *6.1.2)*, we established the thermal limit of stability of Orc_1 at ~450 °C, a temperature at which gersdorffite and nickeline may already coexist in equilibrium (Yund, 1962). This temperature is similar to the equilibration temperatures of ~430 °C estimated by González-Jiménez et al. (2016) for gersdorffite–nickeline in equilibrium with chlorite in pores of metamorphic chromite (see Fig. 6o) in the diopside-bearing antigoritic schistose serpentinites from Lavanderos. All these thermal conditions would prevail inside the subduction channel or during the D2 event of incorporation of the serpentinites at the base of the accretionary prism. Furthermore, the Co-poor nature of these gersdorffites indicates possible sub-solidus equilibration at ≤300 °C (Fig. 13b; Klemm, 1965), which could be contemporary with the D3 event and the crystallization of Orc_2.

Pentlandite (Pn_1) from antigoritic massive serpentinites registers equilibration temperatures ≤200 °C (Fig. 13a), which are lower than the estimated temperature of antigorititization (≥ 300 °C). Textural observations indicate that these pentlandites are commonly replaced by aggregates of smythite–violarite ± magnetite ± pyrite (Fig. 5a-l). Smythite is only stable below 75 °C and usually forms by supergene alteration of pentlandite (e.g., Schwarzenbach et al., 2014 and references therein). Likewise, the reaction of pentlandite with acidic H_2S-bearing fluids at ~80 °C may produce supergene violarite ± pyrite assemblages as those shown in Figs. 5e-f (Tenailleau et al., 2006). The presence of an irarsite inclusion in supergene pyrite (Fig. 5h) suggests that weathering of pentlandite may have also involved certain degree of remobilization of As and Ir. Therefore, from the observations above it seems that Pn_1 in massive antigoritites experienced supergene alteration after exhumation-related metamorphism registered by other Ni-Fe-S-As minerals identified in the la Cabaña ultramafic bodies.

6.2. Evaluating the mineral-scale mobility of (semi)-metals and precious metals

The LA-ICP-MS analyses of some of the larger Hz_1 grains from partially serpentinized massive peridotites yielded lower abundances of Bi but higher of Co, Cd, Os and Ir than Hz_2 from antigoritic schistose serpentinites (Figs. 9a-c and 10a). These differences in trace elements may reflect that Hz_1 formed directly from metals fixed during the hydration of silicates whereas Hz_2 derived from alteration of pre-existing Pn_1. This is supported by the almost identical concentrations of (semi)-metals and precious metals in Hz_2 and Aw_2 from antigoritic schistose serpentinites compared to the precursor Pn_1 (except for slightly lower contents of Co, Pb and Cd in some heazlewoodites) (9a-d). This suggests overall metal immobility during the transformation of pentlandite to awaruite–magnetite (Eq. 2) or heazlewoodite–magnetite (Eq. 3–4). Similarly, Mil_1 in antigoritic schistose serpentinites exhibits chondrite-normalized patterns of (semi)-metals and precious metals identical to Hz_2 they replaced (Fig. 9a-b and 14d-e). It also suggests that sulfurization promoted by increasing fO_2 and fS_2 upon further antigoritization did not significantly disturb the original metal budget either.

Pn_1 in antigoritic massive serpentinites of Loma Guzmán are richer in Bi than Pn_1 in antigoritic schistose serpentinites from Centinela Bajo (Fig. 9c). Interestingly, this positive anomaly is preserved in the smythite replacing the Pn_1 of Loma Guzmán. This enrichment in Bi either fingerprints a distinct composition of the parental fluids that precipitated Pn_1 from Loma Guzmán, or more likely the incorporation of Bi by the highly oxidising and acidic fluids that produced the supergene alteration of this pentlandite. This contrasts with the remarkable depletion of smythite in all (semi)-metals and in particular Ir, Pt and Pd relative to their precursor Pn_1, suggesting that supergene fluids were able to remobilize these precious metals at the mineral scale. The presence of a tiny grain of irarsite within supergene pyrite (Fig. 5h) further evidences this low-temperature remobilization.

No significant geochemical changes were observed between Orc_1 and Orc_2 from different serpentinite lithotypes, except for a slight enrichment in Cu and depletion in Pt in Orc_2 of diopside-bearing antigoritic schistose serpentinites (Fig. 9e). This suggests the persistence of the original signature in arsenides during the entire subduction cycle involving both prograde (burial) and retrograde (exhumation) conditions. The slight differences in Cu and Pt between Orc_1 and Orc_2 may be attributed to an uptake of these elements during recrystallization associated to exhumation during the D_3 deformation phase. We also note that in the diopside-bearing antigoritic schistose serpentinites nickelines are richer in Co, Bi, Te, Pb and Au than coexisting Orc_2 (Fig. 9e-f), which may reflect an additional remobilization of these elements during the final stages of exhumation. The possible sources for gold could be (González-Jiménez et al., 2016): (1) primary gold present in solid solution or as nano to submicron particles within the coexisting magmatic chromite and/or refractory sulfide inclusions in them, and/or (2) mesothermal gold mineralizations in the enclosing metasedimentary rocks remobilized by metamorphic fluids.

Summarizing the interpretations above, (sulf)-arsenides are the main repositories of As and Sb whereas sulfides especially partition Co. These minerals exhibit comparable amounts of Ni and other (semi)-metals such as Te, Pb, Cd, Se, Cu and Zn. Awaruite originated during early

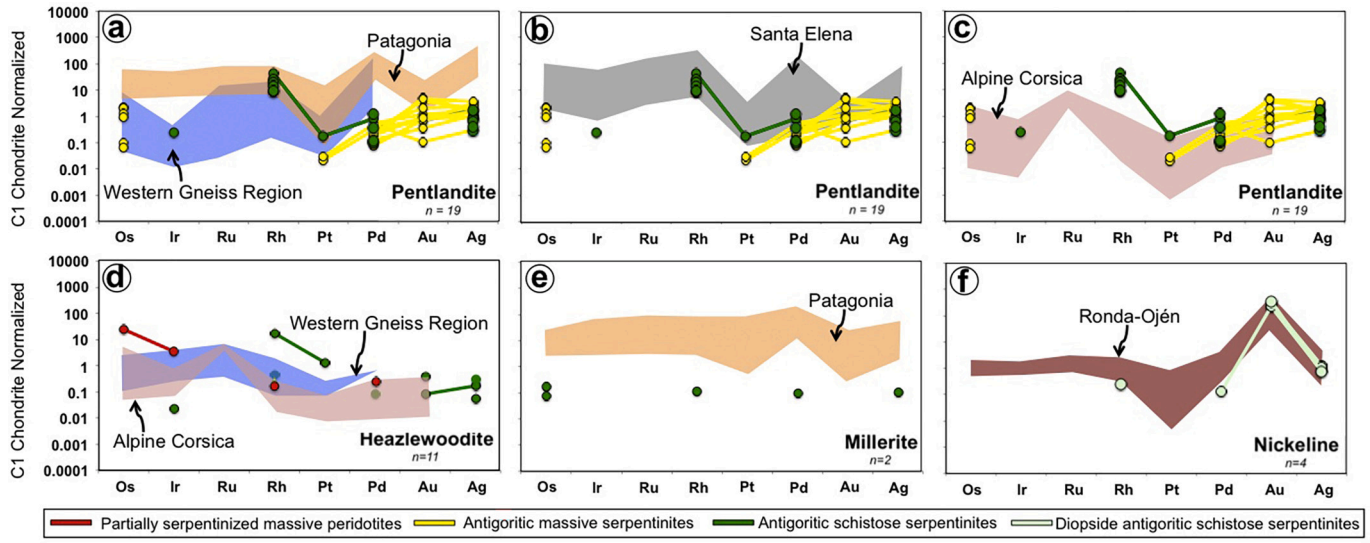

Fig. 14. Chondrite-normalized patterns of precious metals (Os, Ir, Ru, Pt, Au and Ag) of Ni-Fe-S-As minerals from the La Cabaña serpentinites and comparison with equivalent mineral species reported in the literature, including: magmatic pentlandite and heazlewoodite from sub-arc mantle peridotites from the rear of the Andes in the Argentinian Patagonia (Tassara et al., 2018) and the Western Gneiss Region of Norway (Rielli et al., 2018), altered pentlandite from the oceanic peridotites of the Santa Elena ophiolite serpentinized within the ocean floor setting (Holm, 2016), and metamorphic pentlandite and heazlewoodite from subducted serpentinites from the Alpine Corsica (Crossley et al., 2020). Data of magmatic nickeline from ores hosted in peridotites of the SCLM exposed in the Ronda and Ojén ultramafic massif (Piña et al., 2015) from southern Spain are also included for comparison. Normalizing values from McDonough and McDonough and Sun (1995).

stages of lizarditization (i.e., Aw_1) or antigoritization (i.e., Aw_2) may concentrate all these elements in amounts similar to their coexisting or precursor sulfides. Precious metal concentrations in sulfides, alloys and (sulf)-arsenides are comparable, excepting the anomalously high amount of gold in nickeline. This observation suggests that magmatic processes with competing sulfide-arsenide melts (e.g., Piña et al., 2015) did not control precious metal partitioning in subducted serpentinites. Moreover, the budgets of (semi)-metals and precious metals of most Ni–Fe–S–As minerals persist during the entire cycle of subduction-exhumation of serpentinites in the subduction channel. The exception to this rule is Aw_3 formed during high-pressure metamorphism, which exhibits remarkable depletion in Co, Pb, As, Sb, Bi, Te, Cd and Se, as well as precious metals (Fig. 9d and 10d). Such differences in elemental concentrations support the idea that partial dehydration fluids originated under high-temperature and high-pressure metamorphism of serpentinites is able to remobilize at the mineral scale. These fluids probably leached Ni-rich sulfides and arsenides pre-existing in the serpentinite becoming not only enriched in volatile components such as S or Se, and (semi)-metals like As, Sb as previously suggested (Alt et al., 2012; Piccoli et al., 2019), but also in Co, Bi, Te, Cd, Pb as well as precious metals (PGE, Au, Ag). Several natural observations (Barnes and Liu, 2012; González-Jiménez et al., 2010; Levaillant et al., 2016) and experimental works (Mountain and Wood, 1988; Sassani and Schock, 1998) documented that hydrothermal fluids can remobilize Pt, Pd, Au and Ag at the mineral scale. At the P–T–fO_2–fS_2 conditions estimated for the formation of Aw_3 in olivine-bearing mylonitic serpentinites, Pt and Pd might have been extracted as bisulfide and/or hydroxide complexes into fluids with neutral to alkaline pH (e.g., Mountain and Wood, 1988; Sassani and Schock, 1998). Additionally, lower overall (semi)-metal contents in Aw_3 might reflect changes in the alloy structure promoting little ability to carry these elements, although experiments at these P-T conditions are required to confirm this hypothesis.

6.3. *Metamorphic fingerprints of Ni–Fe–S–As minerals in subduction channel serpentinites*

All pentlandite grains analyzed in this study are systematically richer in As, Sb and Pb than pentlandites in unaltered sub-arc peridotites and oceanic peridotites serpentinized at the ocean floor (Fig. 9c). This is consistent with the interpretation given above that the formation of the La Cabaña serpentinites involved the infiltration into mantle peridotites of fluids emanated from meta-sedimentary sources in a subduction zone. Furthermore, pentlandite in La Cabaña serpentinites has similar contents of Os, Ir and Rh but lower Pt, Pd, Au and Ag than pentlandite in unaltered sub-arc peridotites and oceanic serpentinites (Fig. 14a-b). Crossley et al. (2020) observed a similar precious metal decoupling in subducted serpentinites from Alpine Corsica (Fig. 14c), leading to the suggestion that this is a typical fingerprint of pentlandites from subducted serpentinites.

To our knowledge, there are no published LA-ICP-MS data of (semi)-metals in heazlewoodite from unaltered or serpentinized oceanic peridotites in the literature. However, PGE data are available for heazlewoodite hosted in mantle wedge peridotites from the Western Gneiss Region of Norway (Rielli et al., 2018) and subducted serpentinites from Alpine Corsica (Crossley et al., 2020). As a whole, the concentrations of precious metals in the Hz_1 and Hz_2 grains analyzed in this study and these two existing cases are comparable (Fig. 14d). Although the database is not statistically robust, this similarity may evidence comparable immobility of (semi)-metals and precious metals during different styles of serpentinization and subduction.

Similarly, the two millerite grains analyzed in this study using LA-ICP-MS have contents of all (semi)-metals similar to magmatic millerite from sub-arc mantle peridotites (Fig. 9b), although they show slightly higher abundances of As and Sb. However, the two grains analyzed here have lower contents of all precious metals than magmatic millerite (Fig. 14e). Therefore, these observations confirm that relatively high As and Sb contents but low precious metals contents could be a characteristic signature of millerite from subduction channel serpentinites, which distinguish them from igneous millerites present in mantle peridotites.

To date there are not accurate in situ trace element data for Ni—Fe alloys and orcelite in mantle rocks, or for their products of alteration formed during serpentinization within subduction zones. However, in situ trace element data are available for nickeline from magmatic ores of the metasomatized subcontinental lithospheric mantle of the Ronda massif in southern Spain (Piña et al., 2015). Interestingly, nickeline from

La Cabaña and Ronda have identical amounts of Sb, Co, Bi, Te and Se but different concentrations of Cd and Cu (more variable in the Ronda case) (Fig. 9f). The magmatic ones from Ronda have detectable amounts of all precious metals unlike nickeline in La Cabaña serpentinites that only contain traceable contents of Pd, Au and Ag (Fig. 14f). Nevertheless, nickeline from both settings exhibit identical Au—Ag distribution (Fig. 14f). These precious metals concentrations are consistent with solubility limits estimated for these minerals in experiments on the Ni-As-Pd system carried out at 450 °C (Gervilla et al., 1994), suggesting that noble metals were incorporated at their maximum solubility limits in these arsenides. The origin of the Ronda ores has been associated to the interaction of PGE-rich magmas with fluids derived from dehydration of country crustal metasediments when host peridotites were incorporated into the continental crust (Gervilla et al., 2019). As noted above, we also suggest a metasedimentary source for the fluids interacting with the Ni-Fe-S-As minerals in the La Cabaña serpentinite. Therefore, relatively high contents of Sb, Co, Bi, Te and Se and gold are likely a characteristic fingerprint of sulf-arsenides precipitated from fluids with an important meta-sedimentary component.

7. Conclusions

The Ni-rich, S-poor sulfide–alloy (± oxide) assemblages consisting of heazlewoodite ± awaruite ± magnetite in the partially serpentinized massive peridotites from La Cabaña formed during static replacement of magmatic olivine by mesh lizardite. These rocks located in the inner parts of the developing F_1 tubular folds were preserved from the infiltration of slab fluids that caused antigoritization of locally schistose partially serpentinized peridotites and antigoritic schistose serpentinites. In the latter rocks, sulfide ± alloy ± oxide assemblages formed during static antigoritization were deformed and partly re-equilibrated with infiltrating hotter slab-derived fluids. This produced assemblages indicating both decreasing and increasing of fO_2 and fS_2 in the system. These processes of prograde metamorphism did not substantially modify the original trace-elements signatures in the sulfides. Likewise, recrystallization processes associated with exhumation of serpentinites did not affect the distribution of trace-elements in arsenides originated during the earliest stages of static antigoritization, excepting a significant gold enrichment by interaction with fluids from enclosing metasediments of the accretionary prism. In contrast, Ni-rich awaruite in equilibrium with metamorphic olivine-antigorite is depleted in most metals, evidencing their transfer to slab-derived fluids. A comparison of the trace element distribution in the La Cabaña Ni–Fe–S–As minerals with counterparts from other subduction-related peridotites and serpentinites, reveals that Ni–Fe–S–As minerals precipitated from aqueous fluids within the subduction zone have their own characteristic fingerprints. This subduction-related fingerprint is defined by an overall depletion in precious metals and enrichment in As, Sb, Te, Bi and Pb relative to magmatic minerals in unaltered upper mantle peridotites and peridotites serpentinized in ocean basins.

Declaration of Competing Interest

The authors declare that they have no known competing financial interests or personal relationships that could have appeared to influence the work reported in this paper.

Acknowledgements

This research has been funded by the Spanish project RTI2018-099157-A-I00 granted by the “Ministerio de Ciencia, Innovación y Universidades”. Additional funding for chemical analysis was provided by the Ramón y Cajal Fellowship RYC-2015-17596 to JMGJ. Jesús Montes is acknowledged for his careful preparation of the thin-sections. Isabel Sánchez Almazo and Rocío Márquez Crespo (CIC, University of Granada) are also acknowledged for their assistance with HR-SEM and FE-SEM analysis respectively. We are also indebted to Miguel Ángel Hidalgo Laguna (CIC, University of Granada) and Xavier Llovet (Centres Científics i Tecnològics of the Universitat of Barcelona) for their careful help with EPMA.

Appendix A. Supplementary data

Supplementary data to this article can be found online at https://doi.org/10.1016/j.lithos.2021.106432.

References

Agard, P., 2021. Subduction of oceanic lithosphere in the Alps: selective and archetypal from (slow-spreading) oceans. Earth Sci. Rev. 103517.

Alt, J.C., Shanks, W.C., 2003. Serpentinization of abyssal peridotites from the MARK area, Mid-Atlantic Ridge: Sulfur geochemistry and reaction modeling. Geochim. Cosmochim. Acta 67, 641–653. https://doi.org/10.1016/S0016-7037(02)01142-0.

Alt, J.C., Garrido, C.J., Shanks, W.C., Turchyn, A., Padrón-Navarta, J.A., López Sánchez-Vizcaíno, V., Gómez Pugnaire, M.T., Marchesi, C., 2012. Recycling of water, carbon, and sulfur during subduction of serpentinites: a stable isotope study of Cerro del Almirez, Spain. Earth Planet. Sci. Lett. 327–328, 50–60. https://doi.org/10.1016/j.epsl.2012.01.029.

Alt, J.C., Schwarzenbach, E., Früh-Green, G.L., Shanks, W.C., Bernasconi, S.M., Garrido, C.J., Crispini, L., Gaggero, L., Padrón-Navarta, J.A., Marchesi, C., 2013. The role of serpentinites in cycling of carbon and sulfur: Seafloor serpentinization and subduction metamorphism. Lithos 178, 40–54. https://doi.org/10.1016/j.lithos.2012.12.006.

Arai, S., Ishimaru, S., Miura, M., Akizawa, N., Mizukami, T., 2020. Post-Serpentinization Formation of Theophrastite-Zaratite by Heazlewoodite Desulfurization: an Implication for Shallow Behavior of Sulfur in a Subduction complex. Minerals. 10 (9), 806. https://doi.org/10.3390/min10090806.

Barnes, S.J., Liu, W., 2012. Pt and Pd mobility in hydrothermal fluids: evidence from komatiites and from thermodynamic modelling. Ore Geol. Rev. 44, 49–58. https://doi.org/10.1016/j.oregeorev.2011.08.004.

Barra, F., Barnes, J., Reich, M., 2012. The serpentinites from the Coastal Cordillera of south Central Chile — a preliminary report. AGU Fall Meeting Abstracts 1, 2809.

Beard, J., Hopkinson, L., 2000. A fossil, serpentinization-related hydrothermal vent, Ocean Drilling Program Leg 173: College Station, TX (Ocean Drilling Program), Site 1068 (Iberia Abyssal Plain): some aspects of mineral and fluid chemistry. J. Geophys. Res. 105, 16527–16540. https://doi.org/10.1029/2000JB900073.

Bebout, G.E., 2007. Metamorphic chemical geodynamics of subduction zones. Earth Planet. Sci. Lett. 260, 373–393. https://doi.org/10.1016/j.epsl.2007.05.050.

Blanco-Quintero, I.F., Proenza, J.A., García-Casco, A., Tauler, E., Galí, S., 2011. Serpentinites and serpentinites within a fossil subduction channel: La Corea mélange, eastern Cuba. Geol. Acta 9, 389–405. https://doi.org/10.1344/105.000001662.

Buckahr, D.J.M., 1989. Co-Ni-as sulphides in serpentinites of different metamorphic grade in the Eastern Central Alps (Switzerland and Italy). Mineral. Petrol. 41, 65–71. https://doi.org/10.1007/BF01164811.

Cannaò, E., Malaspina, N., 2018. From oceanic to continental subduction: implications for the geochemical and redox evolution of the supra-subduction mantle. Geosphere 14, 6. https://doi.org/10.1130/GES01597.1.

Castro, A., Gerya, T.V., 2008. Magmatic implications of mantle wedge plumes: Experimental study. Lithos 103, 138–148. https://doi.org/10.1016/j.lithos.2007.09.012.

Crossley, R.J., Evans, K.A., Evans, N., Bragagni, A., McDonald, B.J., Reddy, S.M., Speelmanns, I.M., 2020. Tracing highly siderophile elements through subduction: insights form high-pressure serpentinites and ‘hybrid’ rocks from the Alpine Corsica. J. Petrol. 61, 2. https://doi.org/10.1093/petrology/egaa030.

Debret, B., Koga, K.T., Nicollet, C., Andreani, M., Schwartz, S., 2014. F, Cl and S input via serpentinite in subduction zones: implications for the nature of the fluid released at depth. Terra Nova 26, 96–101. https://doi.org/10.1111/ter.12074.

Deckart, K., Hervé, F., Fanning, M., Ramírez, V., Calderón, M.Y., Godoy, E., 2014. U-Pb geochronology and Hf-O isotopes of zircons from the pennsylvanian coastal batholith, south Central Chile. Andean Geol. 41, 49–82. https://doi.org/10.5027/andgeoV41n1-a03.

Deschamps, F., Guillot, S., Godard, M., Chauvel, C., Andreani, M., Hattori, K., 2010. In situ characterization of serpentinites from forearc mantle wedges: timing of serpentinization and behavior of fluid-mobile elements in subduction zones. Chem. Geol. 269, 262–277. https://doi.org/10.1016/j.chemgeo.2009.10.002.

Deschamps, F., Guillot, S., Godard, M., Andreani, M., Hattori, K., 2011. Serpentinites act as sponges for fluid-mobile elements in abyssal and subduction zone environments. Terra Nova 23, 171–178. https://doi.org/10.1111/j.1365-3121.2011.00995.x.

Deschamps, F., Godard, M., Guillot, S., Hattori, K., 2013. Geochemistry of subduction zone serpentinites: a review. Lithos 178, 96–127. https://doi.org/10.1016/j.lithos.2013.05.019.

Eckstrand, O.R., 1975. The Dumont Serpentinite: a model for control of nickeliferous opaque mineral assemblages by alteration reactions in ultramafic rocks. Econ. Geol. 70, 183–201. https://doi.org/10.2113/gsecongeo.70.1.183.

Evans, K.A., Reddy, S.M., Tomkins, A.G., Crossley, R.J., Frost, B.R., 2017. Effects of geodynamic setting on the redox state of fluids released by subducted mantle lithosphere. Lithos 278, 26–42. https://doi.org/10.1016/j.lithos.2016.12.023.

Filippidis, A., 1982. Experimental study of the serpentinizatino of Mg-Fe-Ni olivine in the presence of sulfur. Can. Mineral. 20, 567–574.
Filippidis, A., 1985. Formation of awaruite in the system Ni-Fe-Mg-Si-O-H-S and olivine hydration with NaOH solution, an experimental study. Econ. Geol. 80, 1974–1980. https://doi.org/10.2113/gsecongeo.80.7.1974.
Frost, B.R., 1985. On the stability of sulfides, oxides and native metals in serpentinite. J. Petrol. 25, 31–63. https://doi.org/10.1093/petrology/26.1.31.
Foustoukos, D.I., Bizimis, M., Frisby, C., Shirey, S.B., 2015. Redox controls on Ni-Fe-PGE mineralization and Re/Os fractionation during serpentinization of abyssal peridotite. Geochim. Cosmochim. Acta 150, 11–25. https://doi.org/10.1016/j.gca.2014.11.025.
Gervilla, F., Makovicky, E., Makovicky, M., Rose-Hansen, J., 1994. The system Pd-Ni-as at 790 °C and 450 °C. Econ. Geol. 89, 1630–1639. https://doi.org/10.2113/gsecongeo.89.7.1630.
Gervilla, F., González-Jiménez, J.M., Hidas, K., Marchesi, C., Piña, R., 2019. Geology and metallogeny of the upper mantle rocks from the Serranía de Ronda. Mongraphy of the Spanish Mineralogical Society, 122 pp.
Gerya, T.V., Stöckhert, B., Perchuk, A.L., 2002. Exhumation of high-pressure metamorphic rocks in a subduction channel: a numerical simulation: exhumation of high-pressure rocks. Tectonics 21 (6). https://doi.org/10.1029/2002TC001406 (6-1-6-19).
Gerya, T.V., Yuen, D.A., 2003. Rayleigh - Taylor instabilities from hydration and melting propel "cold plumes" at subduction zones. Earth Planet. Sci. Lett. 212 (1–2), 47–62. https://doi.org/10.1016/S0012-821X(03)00265-6.
González-Jiménez, J.M., Gervilla, F., Kerestedjian, T., Proenza, J.A., 2010. Alteration of Platinum-Group and Base-Metal Mineral Assemblages in Ophiolite Chromitites from the Dobromirtsi Massif, Rhodope Mountains (Bulgaria). Resour. Geol. 60 (4), 315–334. https://doi.org/10.1111/j.1751-3928.2010.00138.x.
González-Jiménez, J.M., Barra, F., Walker, R.J., Reich, M., Gervilla, F., 2014. Geodynamic implications of ophiolitic chromitites in the La Cabaña ultramafic bodies, Central Chile. Int. Geol. Rev. 56, 1466–1483. https://doi.org/10.1080/00206814.2014.947334.
González-Jiménez, J.M., Barra, F., Garrido, L.N.F., Reich, M., Satsukawa, T., Romero, R., Morata, D., 2016. A secondary precious and base metal mineralization in chromitites linked to the development of a Paleozoic accretionary complex in Central Chile. Ore Geol. Rev. 78, 14–40. https://doi.org/10.1016/j.oregeorev.2016.02.017.
González-Jiménez, J.M., Plissart, G., Garrido, L.N.F., Padrón-Navarta, J.A., Aiglsperger, T., Romero, R., Marchesi, C., Moreno-Abril, A.J., Reich, M., Barra, F., Morata, D., 2017. Ticlinohumite and Ti-chondrodite in antigorite serpentinites from Central Chile: evidence for deep and cold subduction. Eur. J. Mineral. 29, 959–970. https://doi.org/10.1127/ejm/2017/0029-2668.
González-Jiménez, J.M., Piña, R., Kerestedjian, T.N., Gervilla, F., Borrajo, I., Farré-de Pablo, J., Proenza, J.A., Tornos, F., Roqué, J., Nieto, F., 2021. Mechanisms for PdAu enrichment in porphyry-epithermal ores of the Elatsite deposit, Bulgaria. J. Geochim. Explor 220, 106664. https://doi.org/10.1016/j.gexplo.2020.106664.
Griffin, W.L., 2008. GLITTER: data reduction software for laser ablation ICP-MS. Laser Ablation ICP-MS in the Earth Sciences 308–311.
Guillot, S., Hattori, K.H., de Sigoyer, J., Nägler, T., Auzende, A.-L., 2001. Evidence of hydration of the mantle wedge and its role in the exhumation of eclogites. Earth Planet. Sci. Lett. 193, 115–127. https://doi.org/10.1016/S0012-821X(01)00490-3.
Guillot, S., Schwartz, S., Reynard, B., Agard, P., Prigent, C., 2015. Tectonic significance of serpentinites. Tectonophysics 646, 1–19. https://doi.org/10.1016/j.tecto.2015.01.020.
Harvey, J., Garrido, C.J., Savov, I., Agostini, S., Padrón-Navarta, J.A., Marchesi, C., López Sánchez-Vizcaíno, V., Gómez-Pugnaire, M.T., 2014. ^{11}B-rich fluids in subduction zones: the role of antigorite dehydration in subducting slabs and boron isotope heterogeneity in the mantle. Chem. Geol. 376, 20–30. https://doi.org/10.1016/j.chemgeo.2014.03.015.
Hattori, K.H., Guillot, S., 2003. Volcanic fronts form as a consequence of serpentinite dehydration in the forearc mantle wedge. Geology 31, 525–528. https://doi.org/10.1130/0091-7613(2003)031<0525:VFFAAC>2.0.CO;2.
Hattori, K.H., Guillot, S., 2007. Geochemical character of serpentinites associated with high to ultrahigh-pressure rocks in the Alps, Cuba, and the Himalayas: recycling of elements in subduction zones. Geochem. Geophys. Geosyst. 8 (9), Q09010 https://doi.org/10.1029/2007GC00159.
Hattori, K.H., Arai, S., Clarke, D.B., 2002. Selenium, tellurium, arsenic and antimony content of primary mantle sulfides. Can. Mineral. 40, 637–650.
Hervé, F., Calderón, M., Fanning, C.M., Pankhurst, R.J., Godoy, E., 2013. Provenance variations in the late Paleozoic accretionary complex of Central Chile as indicated by detrital zircons. Gondwana Res. 23, 1122–1135. https://doi.org/10.1016/j.gr.2012.06.016.
Höfer, C., Kraus, S., Miller, H., Alfaro, G., Barra, F., 2001. Chromite-bearing serpentinite bodies within an arc–backarc metamorphic complex near La Cabaña, south Chilean Coastal Cordillera. J. S. Am. Earth Sci. 14, 113–126. https://doi.org/10.1016/S0895-9811(01)00011-6.
Holm, J.A., 2016. Platinum Decoupling from PGE in Peridotitic Sulfides from the St. Elena Ophiolite in Costa Rica (Master's thesis). http://scholarcommons.sc.edu/etd/3524.
Hyndman, R.D., Peacock, S.M., 2003. Serpentinization of the forearc mantle. Earth Planet. Sci. Lett. 212, 417–432. https://doi.org/10.1016/S0012-821X(03)00263-2.
Hyppolito, T., García-Casco, A., Juliani, C., Meira, V.T., Hall, C., 2014a. Late Paleozoic onset of subduction and exhumation at the western margin of Gondwana (Chilenia Terrane): counterclockwise P–T paths and timing of metamorphism of deep-seated garnet–micha schist and amphibolite of Punta Sirena, Coastal Accretionary Complex, Central Chile (34° S). Lithos 206–207, 409–434. https://doi.org/10.1016/j.lithos.2014.07.023.
Hyppolito, T., Juliani, C., García-Casco, A., Meira, V.T., Bustamante, A., Hervé, F., 2014b. The nature of the Paleozoic oceanic basin at the southwestern margin of Gondwana and implications for the origin of the Chilenia terrane (Pichilemu region, Central Chile). Int. Geol. Rev. 56, 1097–1121. https://doi.org/10.1080/00206814.2014.919612.
Kaneda, H., Takenouchi, S., Shoji, T., 1986. Stability of pentlandite in the Fe–Ni–Co–S system. Mineral. Deposita 21, 169–180. https://doi.org/10.1007/BF00199797.
Kendrick, M.A., Scambelluri, M., Honda, M., Phillips, D., 2011. High abundances of noble gas and chlorine delivered to the mantle by serpentinite subduction. Nat. Geosci. 4, 807–812. https://doi.org/10.1038/ngeo1270.
Klein, F., Bach, W., 2009. Fe–Ni–Co–O–S phase relations in peridotite seawater interactions. J. Petrol. 50, 37–59. https://doi.org/10.1093/petrology/egn071.
Klemm, D.D., 1965. Synthesen und Analysen in den Dreiecksdiagrammen FeAsS–CoAsS–NiAsS und FeS_2–CoS_2–NiS_2. Neues Jahrb. Mineral. Abh. 103, 205–255.
Levaillant, M., Barnes, S.J., Fiorentini, M.L., Santaguida, F., Törmänen, T., 2016. Effects of hydrous alteration on the distribution of base metals and platinum group elements within the Kevitsa magmatic nickel sulphide deposit. Ore Geol. Rev. 72, 128–148. https://doi.org/10.1016/j.oregeorev.2015.06.002.
McDonough, W.F., Sun, S.S., 1995. The composition of the Earth. Chem. Geol. 120, 223–253. https://doi.org/10.1016/0009-2541(94)00140-4.
Mountain, B.W., Wood, S.A., 1988. Chemical controls on the solubility, transport and deposition of platinum and palladium in hydrothermal solutions: a thermodynamic approach. Econ. Geol. 83, 492–511. https://doi.org/10.2113/gsecongeo.83.3.492.
Padrón-Navarta, J.A., López Sánchez-Vizcaíno, V., Garrido, C.J., Gómez-Pugnaire, M.T., 2011. Metamorphic Record of High-pressure Dehydration of Antigorite Serpentinite to Chlorite Harzburgite in a Subduction setting (Cerro del Almirez, Nevado–Filábride complex, Southern Spain). J. Petrol. 52, 2047–2078. https://doi.org/10.1093/petrology/egr039.
Paton, C., Hellstrom, J., Paul, B., Woodhead, J., Hergt, J., 2011. Iolite: Freeware for the visualisation and processing of mass spectrometric data. J. Anal. At. Spectrom. 26, 2508–2518. https://doi.org/10.1039/C1JA10172B.
Paulatto, M., Laigle, M., Galve, A., Charvis, P., Sapin, M., Bayrakci, G., Evain, M., Kopp, H., 2017. Dehydration of subducting slow-spread oceanic lithosphere in the Lesser Antilles. Nature Comm. 8, 15980. https://doi.org/10.1038/ncomms15980.
Piccoli, F., Hermann, J., Pettke, T., Connolly, J.A.D., Kempf, E.D., Duarte, J.F.V., 2019. Subducting serpentinites release reduced, not oxidized, aqueous fluids. Sci. Rep. 9, 19573. https://doi.org/10.1038/s41598-019-55944-8.
Piccoli, F., Ague, J.J., Chu, X., Tian, M., Vitale-Bovarone, A., 2021. Field-Based Evidence for Intra-Slab High-Permeability Channel Formation at Eclogite-Facies Conditions During Subduction. Geochem. Geophys. Geosyst. 22 https://doi.org/10.1029/2020GC009520 e2020GC009520.
Piña, R., Gervilla, F., Barnes, S.-J., Ortega, L., Lunar, R., 2015. Liquid immiscibility between arsenide and sulfide melts: evidence from a LA-ICP-MS study in magmatic deposits at Serranía de Ronda (Spain). Mineral. Deposita 50, 265–279. https://doi.org/10.1007/s00126-014-0534-3.
Plissart, G., González-Jiménez, J.M., Garrido, L.N., Colás, V., Monnier, C., Diot, H., Padrón-Navarta, J.A., 2019. Tectono-metamorphic evolution of subduction channel serpentinites from South-Central Chile. Lithos 336-337, 221–241. https://doi.org/10.1016/j.lithos.2019.03.023.
Proenza, J.A., González-Jiménez, J.M., García-Casco, A., Belousova, E., Griffin, W.L., Talavera, C., Rojas-Agramonte, Y., Aiglsperger, T., Navarro-Ciurana, D., Pujol-Solà, N., Gervilla, F., O'Reilly, S.Y., Jacob, D.E., 2018. Cold plumes trigger contamination of oceanic mantle wedges with continental crust-derived sediments: evidence from chromitite zircon grains of eastern Cuban ophiolites. Geosc. Frontiers 9, 1921–1936. https://doi.org/10.1016/j.gsf.2017.12.005.
Rielli, A., Tomkins, A., Nebel, O., Raveggi, M., Jeon, H., Martin, L., Ávila, J.N., 2018. Sulfur isotope and PGE systematics of metasomatised mantle wedge. Earth Planet. Sci. Lett. 497, 181–192. https://doi.org/10.1016/j.epsl.2018.06.012.
Romero, R., González-Jiménez, J.M., Barra, F., Leisen, M., Garrido, L.N., Talavera, C., Gain, S.E.M., Griffin, W.L., O'Reilly, S.Y., Reich, M., Morata, D., 2018. Timing the tectonic mingling of ultramafic rocks andmetasediments in the southern section of the coastal accretionary complex of Central Chile. Int. Geol. Rev. 60, 2031–2045. https://doi.org/10.1080/00206814.2017.1402377.
Romero, R., Barra, F., Leisen, M., Salazar, E., González-Jiménez, J.M., Reich, M., 2020. Sedimentary provenance of the late Paleozoic metamorphic basement, south-Central Chile: Implications for the evolution of the western margin of Gondwana. Int. Geol. Rev. 62 (5), 598–613. https://doi.org/10.1080/00206814.2019.1627589.
Sassani, D.C., Schock, E.L., 1998. Solubility and transport of platinum-group elements in supercritical fluids: Summary and estimates of thermodynamic properties for ruthenium, rhodium, palladium, and platinum solids, aqueous ions, and complexes to 1000°C and 5 kbar. Geochim. Cosmochim. Acta 62, 2543–2671. https://doi.org/10.1016/S0016-7037(98)00049-0.
Saunders, J.E., Pearson, N.J., O'Reilly, S.Y., Griffin, W.L., 2015. Sulfide metasomatism and the mobility of gold in the lithospheric mantle. Chem. Geol. 410, 149–161. https://doi.org/10.1016/j.chemgeo.2015.06.016.
Saunders, J.E., Pearson, N.J., O'Reilly, S.Y., Griffin, W.L., 2016. Gold in the mantle: the role of pyroxenites. Lithos 244, 205–217. https://doi.org/10.1016/j.lithos.2015.12.008.
Scambelluri, M., Rampone, E., Piccardo, G.B., 2001. Fluid and element cycling in subducted serpentinite: a trace-element study of the Erro–Tobbio high pressure ultramafites (Western Alps, NW Italy). J. Petrol. 42, 55–67. https://doi.org/10.1093/petrology/42.1.55.
Scambelluri, M., Tonarini, S., 2012. Boron isotope evidence for shallow fluid transfer across subduction zones by serpentinized mantle. Geology 40, 907–910. https://doi.org/10.1130/g33233.1.

Schwarzenbach, E.M., Gazel, E., Caddick, M.J., 2014. Hydrothermal processes in partially serpentinized peridotites from Costa Rica: evidence from native copper and complex sulfide assemblages. Contrib. Mineral. Petrol. 168, 1079. https://doi.org/10.1007/s00410-014-1079-2.

Song, Y., Moon, H.S., Chon, H.T., 1995. New occurrence and characterization of Ni-serpentinites in the Kwangcheon area, Korea. Clay Miner. 30, 211–224. https://doi.org/10.1180/claymin.1995.030.3.05.

Tassara, S., González-Jiménez, J.M., Reich, M., Saunders, E., Luguet, A., Morata, D., Grégoire, M., van Acken, D., Schilling, M.E., Barra, F., Nowell, G., Corgne, A., 2018. Highly siderophile elements mobility in the subcontinental lithospheric mantle beneath southern Patagonia. Lithos 314, 579–596. https://doi.org/10.1016/j.lithos.2018.06.022.

Tenailleau, C., Pring, A., Etschmann, B., Brugger, J., Grguric, B., Putnis, A., 2006. Transformation of pentlandite to violarite under mild hydrothermal conditions. Am. Mineral. 91, 706–709. https://doi.org/10.2138/am.2006.2131.

Trommsdorff, V., López-Sánchez Vizcaino, V., Gómez-Pugnaire, M.T., Müntener, O., 1998. High pressure breakdown of antigorite to spinifex-textured olivine and orthopyroxene, SE Spain. Contrib. Mineral. Petrol. 132, 139–148. https://doi.org/10.1007/s004100050412.

Vitale Brovarone, A., Sverjensky, D.A., Piccoli, F., Ressico, F., Giovannelli, D., Daniel, I., 2020. Subduction hides high-pressure sources of energy that may feed the deep subsurface biosphere. Nat. Commun. 11, 3880. https://doi.org/10.1038/s41467-020-17342-x.

Willner, A.P., 2005. Pressure–temperature evolution of a late Palaeozoic paired metamorphic belt in North-Central Chile (34°–35°30′S). J. Petrol. 46, 1805–1833. https://doi.org/10.1093/petrology/egi035.

Yund, R.A., 1962. The system Ni–As–Si phase relations and mineralogic significance. Am. J. Sci. 260, 761–782. https://doi.org/10.2475/ajs.260.10.761.